Draft version June 23, 2025
Typeset using LaTeX default style in AASTeX631

TESS photometry of the nova eruption in V606 Vul: asymmetric photosphere and multiple ejections?

Kirill V. Sokolovsky,[1] Elias Aydi,[2,3] Konstantin Malanchev,[1,4] Colin J. Burke,[5,1] Koji Mukai,[6] Jennifer L. Sokoloski,[7] Brian D. Metzger,[8,9] Kirill E. Atapin,[10] Aleksandre A. Belinski,[10] Yu-Ching Chen,[11,1] Laura Chomiuk,[12] Pavol A. Dubovský,[13] Claude-André Faucher-Giguère,[14] Rebekah A. Hounsell,[15,16] Natalia P. Ikonnikova,[10] Vsevolod Yu. Lander,[10] Junyao Li,[1] Justin D. Linford,[17] Amy J. Mioduszewski,[17] Isabella Molina,[2] Ulisse Munari,[18] Sergey A. Potanin,[10] Robert M. Quimby,[19,20] Michael P. Rupen,[21] Simone Scaringi,[22] Nicolai I. Shatsky,[10] Yue Shen,[1,23] Elad Steinberg,[24] Zachary Stone,[1,25] Andrey M. Tatarnikov,[10] Indrek Vurm[26] And Montana N. Williams[17]

—

Antonio Agudo Azcona,[27] David Boyd,[28] Stewart Bean,[27] Horst Braunwarth,[27] John Blackwell,[29] Simone Bolzoni,[27,30] Ricard Casas,[27] David Cejudo Fernandez,[27] Franky Dubois,[31,32] James Foster,[27] Rafael Farfán,[27] Charles Galdies,[33] John Hodge,[34] Jose Prieto Gallego,[27] David J. Lane,[35,30] Magnus Larsson,[27] Peter Lindner,[27] Ludwig Logie,[31,32] Andrea Mantero,[27] Mario Morales Aimar,[27] Kenneth Menzies,[27] Keith Nakonechny,[27] Jerry Philpot,[27] Antonio Padilla Filho,[27] Brian Ramey,[27] Steve Rau,[31,32] Esteban Reina,[27] Filipp D. Romanov,[27,30] Nello Ruocco,[36] Jeremy Shears,[27] Marc Serreau,[27] Richard Schmidt,[27] Yuri Solomonov,[27] Bob Tracy,[27] Gord Tulloch,[27] Ray Tomlin,[27] Tamás Tordai,[27] Siegfried Vanaverbeke[31,32] And Klaus Wenzel[27]

(AAVSO)

Alessandro Maitan[37] And Stefano Moretti[37]

(ANS)

[1] *Department of Astronomy, University of Illinois at Urbana-Champaign, 1002 W. Green Street, Urbana, IL 61801, USA*
[2] *Center for Data Intensive and Time Domain Astronomy, Department of Physics and Astronomy, Michigan State University, 567 Wilson Rd, East Lansing, MI 48824, USA*
[3] *Department of Physics & Astronomy, Texas Tech University, Box 41051, Lubbock, TX 79409-1051, USA*
[4] *McWilliams Center for Cosmology & Astrophysics, Department of Physics, Carnegie Mellon University, Pittsburgh, PA 15213, USA*
[5] *Department of Astronomy, Yale University, 266 Whitney Avenue, New Haven, CT 06511, USA*
[6] *CRESST and X-ray Astrophysics Laboratory, NASA/GSFC, Greenbelt, MD 20771, USA*
[7] *Columbia Astrophysics Laboratory, Columbia University, New York, NY 10027, USA*
[8] *Department of Physics and Columbia Astrophysics Laboratory, Columbia University, New York, NY 10027, USA*
[9] *Center for Computational Astrophysics, Flatiron Institute, 162 5th Ave, New York, NY 10010, USA*
[10] *Sternberg Astronomical Institute, Moscow State University, Universitetskii pr. 13, 119992 Moscow, Russia*
[11] *Department of Physics and Astronomy, Johns Hopkins University, Baltimore, MD 21218, USA*
[12] *enter for Data Intensive and Time Domain Astronomy, Department of Physics and Astronomy, Michigan State University, 567 Wilson Rd, East Lansing, MI 48824, USA*
[13] *Vihorlat Astronomical Observatory, Mierová 4, 066 01 Humenné, Slovakia*
[14] *CIERA and Department of Physics and Astronomy, Northwestern University, 1800 Sherman Ave, Evanston, IL 60201, USA*
[15] *University of Maryland, Baltimore County, Baltimore, MD 21250, USA*
[16] *NASA Goddard Space Flight Center, Greenbelt, MD 20771, USA*
[17] *National Radio Astronomy Observatory, Domenici Science Operations Center, 1003 Lopezville Road, Socorro, NM 87801, USA*
[18] *INAF Astronomical Observatory of Padova, 36012 Asiago (VI), Italy*
[19] *Department of Astronomy and Mount Laguna Observatory, San Diego State University, San Diego, CA 92182, USA*
[20] *Kavli Institute for the Physics and Mathematics of the Universe (WPI), The University of Tokyo Institutes for Advanced Study, The University of Tokyo, Kashiwa, Chiba 277-8583, Japan*
[21] *National Research Council, Herzberg Astronomy and Astrophysics, 717 White Lake Rd, PO Box 248, Penticton, BC V2A 6J9, Canada*
[22] *Centre for Extragalactic Astronomy, Department of Physics, Durham University, South Road, Durham, DH1 3LE, UK*
[23] *National Center for Supercomputing Applications, University of Illinois at Urbana-Champaign, Urbana, IL 61801, USA*

Corresponding author: Kirill Sokolovsky
kirx@kirx.net

[24] *Racah Institute of Physics, The Hebrew University, 9190401 Jerusalem, Israel*
[25] *Center for AstroPhysical Surveys, National Center for Supercomputing Applications, University of Illinois at Urbana-Champaign, Urbana, IL 61801, USA*
[26] *Tartu Observatory, University of Tartu, Tõravere, 61602 Tartumaa, Estonia*
[27] *AAVSO Observer*
[28] *BAA Variable Star Section, West Challow Observatory, OX12 9TX, UK*
[29] *Phillips Exeter Academy, 20 Main Street, Exeter, New Hampshire 03833, USA*
[30] *Abbey Ridge Observatory, 45 Abbey Rd, Stillwater Lake, NS, B3Z1R1 Canada*
[31] *AstroLAB IRIS, Provinciaal Domein "De Palingbeek", Verbrandemolenstraat 5, B-8902 Zillebeke, Ieper, Belgium*
[32] *Vereniging Voor Sterrenkunde (VVS), Oostmeers 122 C, B-8000 Brugge, Belgium*
[33] *Institute of Earth Systems, University of Malta, MSD2080, Malta*
[34] *AAVSO Observer; Bethune Observers Group, Post Office Box 25553, Columbia, South Carolina, 29224, USA*
[35] *Burke-Gaffney Observatory, Saint Mary's University, 923 Robie Street, Halifax, NS B3H 3C3, Canada*
[36] *Osservatorio Astronomico Nastro Verde, Sorrento, Naples, Italy*
[37] *ANS Collaboration, c/o Astronomical Observatory, 36012 Asiago (VI), Italy*

ABSTRACT

Lightcurves of many classical novae deviate from the canonical "fast rise — smooth decline" pattern and display complex variability behavior. We present the first *TESS*-space-photometry-based investigation of this phenomenon. We use Sector 41 full-frame images to extract a lightcurve of the slow Galactic nova V606 Vul that erupted nine days prior to the start of the *TESS* observations. The lightcurve covers the first of two major peaks of V606 Vul that was reached 19 days after the start of the eruption. The nova reached its brightest visual magnitude $V = 9.9$ in its second peak 64 days after the eruption onset, following the completion of Sector 41 observations. To increase the confidence level of the extracted lightcurve, we performed the analysis using four different codes implementing the aperture photometry (LIGHTKURVE, VaST) and image subtraction (TESSREDUCE, TEQUILA_SHOTS) and find good agreement between them. We performed ground-based photometric and spectroscopic monitoring to complement the *TESS* data. The *TESS* lightcurve reveals two features: periodic variations (0.12771 d, 0.01 mag average peak-to-peak amplitude) that disappeared when the source was within 1 mag of peak optical brightness and a series of isolated mini-flares (with peak-to-peak amplitudes of up to 0.5 mag) appearing at seemingly random times. We interpret the periodic variations as the result of azimuthal asymmetry of the photosphere engulfing the nova-hosting binary that was distorted by and rotating with the binary. Whereas we use spectra to associate the two major peaks in the nova lightcurve with distinct episodes of mass ejection, the origin of mini-flares remains elusive.

Keywords: Classical novae(251) — Photometry(1234) — Stellar winds(1636) — Shocks(2086)

1. INTRODUCTION

1.1. *Novae overview*

A classical nova is an explosive event that occurs on a white dwarf accreting matter from its companion main sequence star in a binary system. As the layer of accreted hydrogen-rich matter builds up on the surface of the white dwarf, the pressure and temperature at the bottom of the layer increase. At a certain point, the pressure and temperature become high enough to lift the electron degeneracy restarting hydrogen fusion (e.g., Bode & Evans 2008a; Starrfield et al. 2016, 2020; Della Valle & Izzo 2020). The energy released by the nuclear reactions leads to a dramatic expansion of the white dwarf atmosphere that engulfs the binary system and is eventually ejected at velocities of $\sim$500–5000 km s^{-1} (Pickering 1895; McLaughlin 1956; Aydi et al. 2020a).

The expanding nova envelope causes the optical brightness of the binary system to increase by $\sim$ 8–15 mag (Vogt 1990; Bode & Evans 2008b; Kawash et al. 2021; with the extreme nova V1500 Cyg having an amplitude $>$ 18 mag; Lindegren & Lindgren 1975) reaching peak absolute magnitudes in the range of -4 to -10 mag (Shafter 2017; Shafter et al. 2009; Schaefer 2022a). As the ejected nova envelope dissipates, the optical brightness of the system declines on timescales of days (Darnley et al. 2016) to months (Strope et al. 2010). The nuclear burning on the white

dwarf manifested by "super-soft source" X-ray emission (SSS; Schwarz et al. 2011; Ness et al. 2013) continues on similar or even longer timescales until the hydrogen fuel is exhausted.

Despite the harsh radiation environment produced by the hot white dwarf, some novae form dust in their envelopes producing the characteristic "dust dip" in the lightcurve that may obscure the system for months before the dust clears (Bode & Evans 2008a; Derdzinski et al. 2017). It may take decades for a nova-hosting binary to reach pre-outburst magnitudes as the eruption leaves the binary in an elevated accretion-rate state. About 30 nova eruptions are estimated to occur in the Galaxy per year (Shafter 2017; De et al. 2021; Kawash et al. 2022; Rector et al. 2022; Zuckerman et al. 2023).

1.2. *Nova envelope and wind*

While some researchers argue that spectroscopic and photometric evolution of a nova may be understood in the framework of a single ballistic ejection event (Shore 2012, 2013; Mason et al. 2018, 2020), others suggest that nova ejecta may contain at least two distinct components (Mclaughlin 1947; Friedjung 1987; Aydi et al. 2020a). The first component comprises the inflated atmosphere of the white dwarf that envelopes the binary, thereby forming a common envelope (Livio et al. 1990; Sparks & Sion 2021; Shen & Quataert 2022). This envelope remains marginally bound to the system and produces low-velocity outflows concentrated towards the binary's orbital plane (Pejcha et al. 2016a; Shen & Quataert 2022). The second component of the circumbinary material is a fast, radiation-driven wind originating from the hot white dwarf (Friedjung 1990; Kato & Hachisu 1994; Friedjung 2004; Shaviv 2001, 2002a; Aydi et al. 2020b). The disruption of the expanded white dwarf atmosphere's outer regions by the binary companion could facilitate the production of the fast wind (Shen & Quataert 2022). The interface between the fast wind and the slow, orbital-plane-focused envelope may be the site of shock formation (Chomiuk et al. 2014, 2021a; Mukai & Sokoloski 2019).

Shocks play a major role in transporting energy within nova ejecta (Chomiuk et al. 2021a). The exact origin and location of the shocks is being debated (Shen & Quataert 2022; Hachisu & Kato 2022; Quimby et al. 2024). The presence of shocks in novae is clearly established by the observations of GeV (Abdo et al. 2010; Ackermann et al. 2014; Franckowiak et al. 2018) and TeV γ-rays (Metzger et al. 2016; Acciari et al. 2022; H. E. S. S. Collaboration et al. 2022), hard ($kT > 1$ keV) thermal X-rays (Nelson et al. 2019; Sokolovsky et al. 2020; Gordon et al. 2021; Sokolovsky et al. 2022a) and non-thermal radio emission (Giroletti et al. 2020; Chomiuk et al. 2021b; Munari et al. 2022a; Sokolovsky et al. 2023). The presence of shocks is also implied by optical spectroscopy that reveals high ionization lines (presumably originating in shock-heated plasma; Gorbatskii 1972; Shields & Ferland 1978; Contini & Prialnik 1997) and multiple outflows launched at different stages of nova eruption with different velocities (that should collide producing shocks; Aydi et al. 2020a; Steinberg & Metzger 2020).

The shocks may directly contribute to optical emission of novae (Metzger et al. 2014) as indicated by the observations of correlated variability in GeV and optical bands (Li et al. 2017; Aydi et al. 2020b). Reprocessed shock emission visible in the optical band may reflect the time evolution of the nova wind properties (Martin et al. 2018).

1.3. *V606 Vul – Nova Vulpeculae 2021*

The eruption of V606 Vul (Nova Vulpeculae 2021, TCP J20210770+2914093, AT 2021twr, PGIR21gds, ZTF21abmbzax) was discovered on 2021-07-16.475 UTC (JD 2459411.975) by Koichi Itagaki as a 12 mag transient source that appeared on images obtained with a 180 mm telephoto lens attached to a CCD camera. The discovery was reported via the Central Bureau for Astronomical Telegrams' Transient Objects Confirmation Page and spectroscopically confirmed as a classical nova by R. Leadbeater (Itagaki et al. 2021) and (Munari et al. 2021b,a). The astrometry reported in Itagaki et al. (2021) allows to identify the nova host: Gaia DR3 1861166838700691968 ($G = 21.05 \pm 0.02$, $BP = 21.37 \pm 0.21$, $RP = 20.59 \pm 0.30$)

```
20:21:07.7044  +29:14:09.091
```

equinox J2000.0, mean epoch 2016.0; with the positional uncertainty of 19 and 17 mas in R.A. and Dec. directions, respectively, with no measured proper motion and parallax (Gaia Collaboration et al. 2016, 2023).

The immediate vicinity of V606 Vul is relatively uncrowded: there are no Gaia DR3 stars brighter than $G = 17.37$ ($RP = 16.37$) within a $60'' \times 60''$ arcsec box centered on the nova (corresponding to the aperture size in § 2.1.3, 2.1.5 and 2.1.6). Any of these stars is at least 5 magnitudes fainter than the faintest magnitude of V606 Vul during the *TESS* Sector 41 observations. Even if brightness of one of these field stars was 100% modulated, this would have produced

a feature with an amplitude < 0.01 mag in the combined lightcurve. We also used the VaST code discussed in § 2.1.4 to analyze 842 ZTF (see § 2.2) r-band images of the field and confirm that there are no high-amplitude variable stars within the box.

1.4. *Scope of this work*

The *Transiting Exoplanet Survey Satellite* (*TESS*) is uniquely equipped for studying Galactic nova eruptions expanding our knowledge of nova lightcurves in two ways. First, thanks to its high photometric precision we can characterize brightness variations in a nova with the amplitudes so low that they cannot be detected from the ground. Second, the space platform's ability to conduct virtually uninterrupted observations over the duration of a month allow one to probe variability on a 12–24 h timescale that is difficult to access with ground-based observations interrupted by the diurnal cycle.

We use *TESS* photometry of the V606 Vul eruption to characterize variability of a nova in exquisite details. As there are other novae that already have and will be erupting in the *TESS* field of view, we present a detailed discussion of technical details associated with measuring a high variability amplitude target with *TESS*. We hope that this work will pave the way for future studies of novae with *TESS*. Section 2 describes the *TESS* data reduction and the supporting ground-based photometry and spectroscopy of V606 Vul. Section 3 presents the observational results. Our interpretation of the observations is discussed in Section 4. We summarize the results in Section 5

While preparing this manuscript, we learned about Luna et al. (2024) analysis of the *TESS* lightcurve of V1674 Her – an exceptionally fast nova that started displaying strong orbital modulation early in its decline. Earlier, Schaefer (2022b, 2023a); Bruch (2023a,b) used *TESS* photometry to characterize orbital periods of multiple nova-hosting systems near quiescence.

2. OBSERVATIONS AND ANALYSIS

2.1. *TESS photometry*

2.1.1. *TESS instrument overview*

TESS is the space mission launched by NASA in 2018 with the aim of discovering transiting exoplanets around bright stars by performing an all-sky photometric survey (Ricker et al. 2015). It operates in a highly eccentric, 2:1 lunar resonance orbit that provides a benign thermal and radiation environment as the spacecraft does not enter the Van Allen Belts (Gangestad et al. 2013). The satellite is equipped with four identical cameras (105 mm aperture, f/1.4 focal ratio) each projecting a $24^\circ \times 24^\circ$ field of view on a 2×2 mosaic of 2048×4096 frame transfer CCDs (Krishnamurthy et al. 2019). The cameras are red-sensitive covering the wavelength range of 6000–10000 Å.

During science operations, the *TESS* cameras produce a continuous stream of images with an exposure time of 2 s. The rapid shutterless readout takes only 4 ms. The images are stacked onboard to produce full-frame images (FFI) with an exposure time of 3 to 30 min (varied over the mission lifetime). Cosmic ray rejection is performed during stacking by considering values obtained at each pixel in $N = 10$ exposures, discarding the highest and lowest of the N values and adding the sum of the remaining values to the stack. This procedure reduces the effective exposure by a factor of $(N-2)/N$ (Vanderspek et al. 2018) and results in the scatter of photometric measurements extracted from the FFIs being *smaller* than what would be naively expected from the Poisson noise. This is in contrast to ground-based observations where systematic effects typically result in the measurement scatter larger than expected for random noise (e.g., Skowron et al. 2016).

TESS tracks the position of 200 bright, isolated guiding stars imaged by its cameras to maintain sub-pixel pointing accuracy (Nguyen 2018). The spacecraft attitude is maintained with four reaction wheels that periodically need to be unloaded (typically twice per orbit, more often during the first years of the mission) by firing hydrazine thrusters – the events that temporarily degrade pointing accuracy.

The science operations are interrupted by ground contacts for data downlink (during a perigee pass) and spacecraft housekeeping (at perigee and apogee). The spacecraft reorientation required to point its high-gain antenna towards a ground station changes the temperature of the cameras by 1-2° C. It takes 1.5–2 days for the temperatures to return to nominal values. With its four cameras *TESS* observes a $96^\circ \times 24^\circ$ strip of the sky (with $\sim 10'$ gaps between the fields covered by the cameras and individual CCD chips) for two orbits before moving to the next strip. Such a month-long observing campaign is referred to as "Sector".

The eruption of V606 Vul was imaged by *TESS* during the observations of Sector 41 between 2021-07-24 11:39:01 ($t_0 + 9$ days) and 2021-08-20 01:49:00 TDB ($t_0 + 36$ days). The nova was in the field of view of Camera 1, CCD 4. The

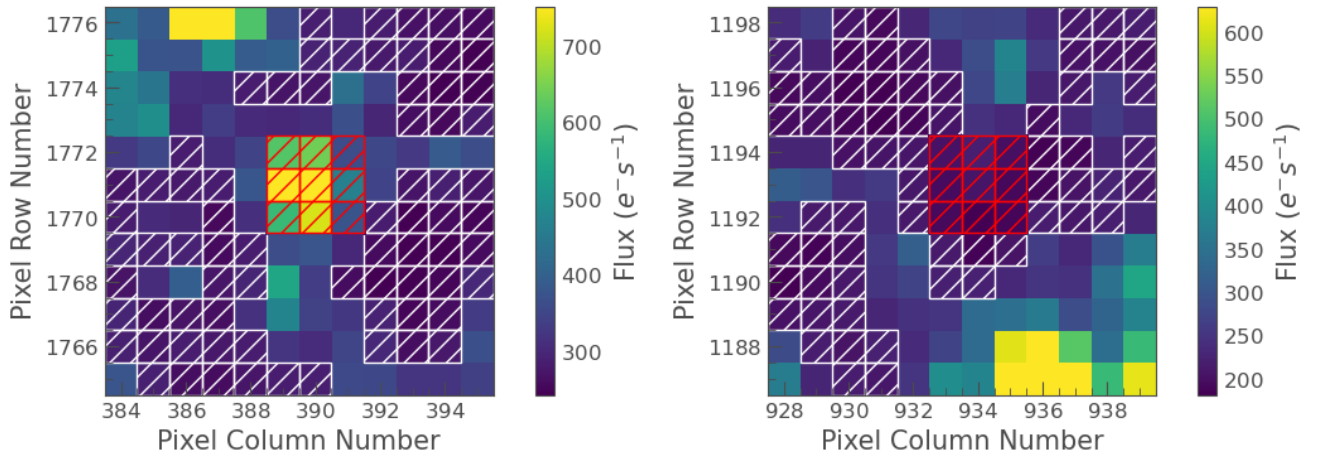

Figure 1. The *TESS* images of the V606 Vul field showing it during the eruption (Sector 41, left) and after it faded (Sector 55, right). The first useful cadence (image) of the sector is displayed in both cases. The red hatched area marks the source aperture and the white hatched area marks the background aperture used in LIGHTKURVE analysis described in § 2.1.3. The nova is clearly visible in Sector 41 but is below the background level in this crowded sky region in Sector 55.

observing cadence in Sector 41 was 600 s, reduced to 475 s effective exposure due to the cosmic ray rejection procedure described above. Apart from Sector 41, the nova was in the *TESS* field of view in Sectors 14 and 15 (2019-07-18 to 2019-09-10) prior to eruption and Sectors 55 (2022-08-05 to 2022-09-01), 81 and 82 (2024-07-15 to 2024-08-29) post-eruption. However, no useful data could be extracted from these additional sectors as the nova was much fainter than the local background at these times (Figure 1).

2.1.2. *Systematic effects in* TESS *photometry*

The brightness measurements in astronomical images are affected by random noise and various systematic effects. *Additive systematic effects* include bias level variations, cross-talk, scattered light, ghost images, and corner glow. These effects can be corrected by carefully estimating the background level and subtracting it from the pixel values. Cosmic ray desaturation manifesting itself as time-dependent elevated dark current in individual pixels – a major concern for *CoRoT* (Pinheiro da Silva et al. 2008; Aigrain et al. 2009), *BRITE* (Pablo et al. 2016; Popowicz & Farah 2020) and the *Hubble Space Telescope* (Sirianni et al. 2007) photometry – does not seem to be affecting *TESS* data thanks to a combination of lower operating CCD temperature and frequent readout. *Multiplicative effects* change the fraction of the incident photons that get detected. While the pixel-to-pixel sensitivity variations are corrected with flatfielding, non-uniform sensitivity within each individual pixel combined with the residual sub-pixel jitter in *TESS* pointing introduce systematic drifts in lightcurves.

Both exoplanet transit and asteroseismology (Handberg et al. 2021) studies require detection of low-amplitude periodic signals in photometry corrupted by systematic effects. A variety of filters may be applied to a lightcurve to suppress instrumental and astrophysical variability on timescales far from those where the periodic signals of interest are expected (Hippke et al. 2019). The key feature of systematic variations is that they affect (to various extent) multiple sources in the field. This may be used to remove systematic trends more efficiently than what is possible to achieve by filtering the target source lightcurve alone.

Inspired by the algorithms developed for ground-based transit surveys such as the Trend Filtering Algorithm (Kovács et al. 2005; Kim et al. 2009; Gopalan et al. 2016) and SysRem (Tamuz et al. 2005; Mazeh et al. 2007), the common approach to detrending is to approximate the target source lightcurve as a linear combination of a set of basis functions representing various systematic effects. The optimal combination can be subtracted from the lightcurve and the residuals searched for a periodic signal, or the model signal can be fit together with the basis functions to the original lightcurve. The basis functions may be the lightcurves of other stars in the field, lightcurves of individual pixels (imaging other sources and background) away from the target source or external engineering information about the spacecraft pointing. The de-trending may be applied to individual pixel rather than source lightcurves (Deming et al. 2015). A clever regularization, cross-validation and modeling of source-intrinsic variability may be needed to construct the smoothest-possible target source lightcurve (Luger et al. 2018; Hattori et al. 2022).

The detrending techniques based on linear regression against a set of basis functions are not easily applicable to highly variable sources like novae and supernovae (e.g., Vallely et al. 2021) because the high variability amplitude cannot be absorbed in the noise term of the regression problem. In other words, the typical de-trending approach is to construct (one way or the other) a simplified model of the observed lightcurve aiming to capture the instrumental effects (like long-term lightcurve trends) while leaving out the signal of interest (like transits). The model is then subtracted from the observed lightcurve to obtain the corrected lightcurve. This works well when the signal of interest has low amplitude compared to the instrumental systematics. However, if true astrophysical variability dominates the observed lightcurve, even a coarse approximation of that lightcurve will capture mostly the astrophysical signal rather than instrumental systematics. Subtracting such a model from the observed lightcurve will necessarily distort the astrophysical variability signal. One could model the astrophysical variability along with the instrumental systematics (for example, modeling an early lightcurve of a supernova as a cubic polynomial; Hattori et al. 2022) but this is not always feasible when little is known about the variability behavior of a target source (like if it can be well represented by a cubic polynomial).

To avoid distorting the target variability pattern, any corrections applied to the target source lightcurve must be determined without involving the target source lightcurve itself. The background subtraction is the most basic correction. The lightcurves of other sources in the field may be used to estimate the level of remaining uncorrected systematics.

To gain confidence in the results we compare multiple techniques of extracting *TESS* photometry (the approach also adopted by Poore & Carini 2023). These techniques and codes implementing them are discussed in the following subsections. We stress that we do not apply any systematics removal technique to the lightcurves: no `RegressionCorrector`, no `PLDCorrector`. An example of how a blind application of such correction may completely distort the lightcurve is presented online[1].

2.1.3. *Aperture photometry with* LIGHTKURVE

LIGHTKURVE (Lightkurve Collaboration et al. 2018) is a PYTHON package for analyzing data from NASA's space photometry missions *Kepler*, *TESS* and future *Roman*. It is based on ASTROPY (Astropy Collaboration et al. 2022) and relies on TESSCUT (Brasseur et al. 2019) to access cutouts of *TESS* FFIs online applying hard (`quality_bitmask=7407`) filtering on the quality flags. The target pixel files (similar to the ones produced by the mission for the pre-selected high-cadence monitoring targets) are created from the FFI cutouts by LIGHTKURVE.

We analyzed a small 12×12 pix cutout centered on the nova position (Figure 1). The nova photometry was extracted from a 3×3 pix square aperture that was centered on the nova using the WCS solution in the cutout FITS image header. We applied `create_threshold_mask(threshold=0.001, reference_pixel=None)` (also excluding the target aperture) to create background measurement mask covering the darkest pixels in the cutout that are likely to be less contaminated by starlight. The background lightcurve was scaled by the relative number of pixels in the background and target apertures and subtracted from the target lightcurve. The resulting lightcurve is presented in Figure 2 and some of its features are highlighted in Figure 3. Appendix A details how timestamps are assigned for each photometric point. A JUPYTER NOTEBOOK implementing the lightcurve extraction is available online[1].

2.1.4. *Aperture photometry with* VAST

VAST is a *general-purpose* photometry pipeline designed to process direct images of the sky (Sokolovsky & Lebedev 2018). The input images may be shifted and rotated with respect to each other. They do not need to have a WCS solution as the code will match stars detected at the reference image to the ones found at all the subsequent images by identifying similar triangles of stars. It can handle images obtained with a wide variety of ground- and space-based telescopes and detectors, including the ones having non-linear response to the number of incoming photons, such as digitized photographic plates (Kolesnikova et al. 2008; Antipin et al. 2018; Sokolovsky et al. 2019) and micro-channel plate intensified CCD (Sokolovsky 2009; Gupta et al. 2012; Rani et al. 2017). Trivial modifications of the code allowed VAST to understand the observing time (Appendix A) and properly handle multi-extension `FITS` files, enabling us to apply VAST to *TESS* full-frame images. Being an established, reasonably well-tested code familiar to the lead author, the VAST analysis described below serves as a cross-check for the *TESS*-specific codes.

[1] https://github.com/kirxkirx/v606vul_lightkurve/

VaST uses SExtractor (Bertin & Arnouts 1996) for independent source detection and photometry in each input image. VaST then matches the star lists produced by SExtractor. To ensure consistency in the magnitude scale of the input images, VaST constructs a magnitude-magnitude relation for all stars identified between pairs of images and approximates it using a function appropriate for the detector type (digitized photographic plates or image intensifiers may require a non-linear calibration function).

We tested various magnitude calibration functions and found that the simple linear function with the slope fixed to 1.0 and a variable intercept (i.e., that accounts only for the variations of magnitude zero-point) minimizes the lightcurve scatter when processing *TESS* FFIs. The variations of *TESS* zero-point between the images are found to be very small: 0.0004 mag r.m.s. As VaST naturally accounts for shifts between the images, it has no problem processing images affected by pointing uncertainties which were found to be extremely small. The measured centroid position of V606 Vul image was stable within 0.10 pix (0.03 pix r.m.s.)

We apply VaST to 3668 full single-chip images obtained with CCD 4 of *TESS* Camera 1 during observations of Sector 41. A total of 3665 images passed VaST built-in quality cuts. The overscan image regions were excluded from the analysis by generating an appropriate weight image supplied to SExtractor. We excluded from the photometric calibration all stars marked as blended (SExtractor `flag>1`). The following command line was used to run the analysis:

```
./vast --UTC --nofind --type 2 --aperture 2.75 \
--autoselectrefimage \
--no_position_dependent_correction \
/data/v606_vul_ffi/tess*-s0041-1-4-*_ffic.fits
```

VaST uses circular apertures centered on independently determined source positions in each image. Larger apertures capture more source light, but also more noise and light from unrelated nearby sources. Smaller apertures capture less source light, reducing signal-to-noise ratio. An optimal aperture size can also vary with seeing, which is a concern for ground-based observations affected by atmospheric turbulence as well as for spaceborne data affected by thermal focus changes and spacecraft pointing jitter. To find an optimal aperture size we repeatedly run the analysis with a range of aperture diameters and choose the one that provides the smoothest lightcurve for V606 Vul as quantified by

$$\frac{1}{\eta} = \frac{\sigma^2}{\delta^2} = \frac{\sum_{i=1}^{N}(m_i - \bar{m})^2/(N-1)}{\sum_{i=1}^{N-1}(m_{i+1} - m_i)^2/(N-1)}, \quad (1)$$

where σ is the standard deviation of the N magnitude measurements m_i, while δ is the mean difference between consecutive m_i, $\bar{m}$ is the mean magnitude (von Neumann 1941, 1942; Sokolovsky et al. 2017; Calamida et al. 2022). The lightcurve obtained with a circular aperture that is 2.75 pixels in diameter was found to be the smoothest one and is used for comparison with the *TESS*-specific photometry codes (§ 3.1).

2.1.5. *Difference image analysis with* TEQUILA_SHOTS

We constructed a lightcurve of V606 Vul using a custom-built *TESS* difference image photometry pipeline TEQUILA_SHOTS (Burke et al. 2020) based on PyZOGY (Guevel & Hosseinzadeh 2017) image subtraction code implementing the algorithm of Zackay et al. (2016) (the previous version of the code described by Burke et al. 2020 was relying on HOTPANTS; Becker 2015). TEQUILA_SHOTS reads a local copy of calibrated FFIs that were downloaded from MAST and uses REPROJECT to make cutouts resampled to the new coordinate grid centered on the target source. The reference image is constructed by median-stacking 20 frames taken near the center of the first orbit in the sector – a time when the contamination from scattered light of the Earth and Moon is expected to be low. We use `photutils.psf.EPSFBuilder` (Anderson & King 2000) to reconstruct the point spread function (PSF) of the reference and each of the individual images. The background-subtracted reference and science images together with the corresponding PSF models are supplied to PyZOGY that constructs optimal difference image for each science image. Unlike other image subtraction algorithms (Phillips & Davis 1995; Alard & Lupton 1998; Bramich 2008; Hitchcock et al. 2021) the algorithm of Zackay et al. (2016) relies on cross-convolution (reference image is convolved with science image PSF and science image is convolved with reference image PSF, extending the approach of

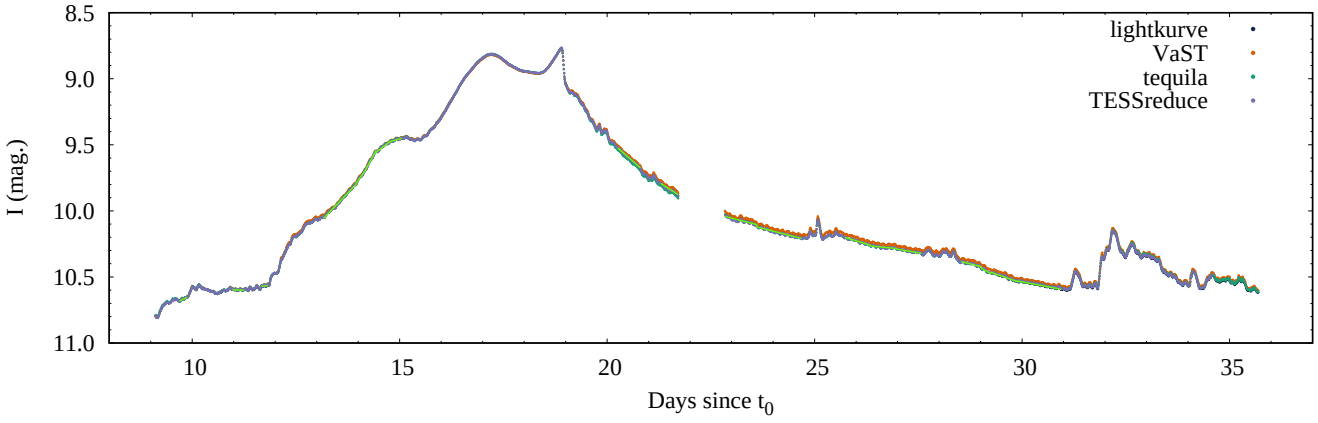

Figure 2. The *TESS* lightcurve of V606 Vul. The same *TESS* full-frame images were measured using four different photometry codes as discussed in § 2.1 and the resulting lightcurves are plotted in different colors. The bright-green lines represent piecewise linear function used to detrend the lightcurve before the period search (§ 3.3). The measurements that do not overlap in time with any of the lines were excluded from the periodicity analysis.

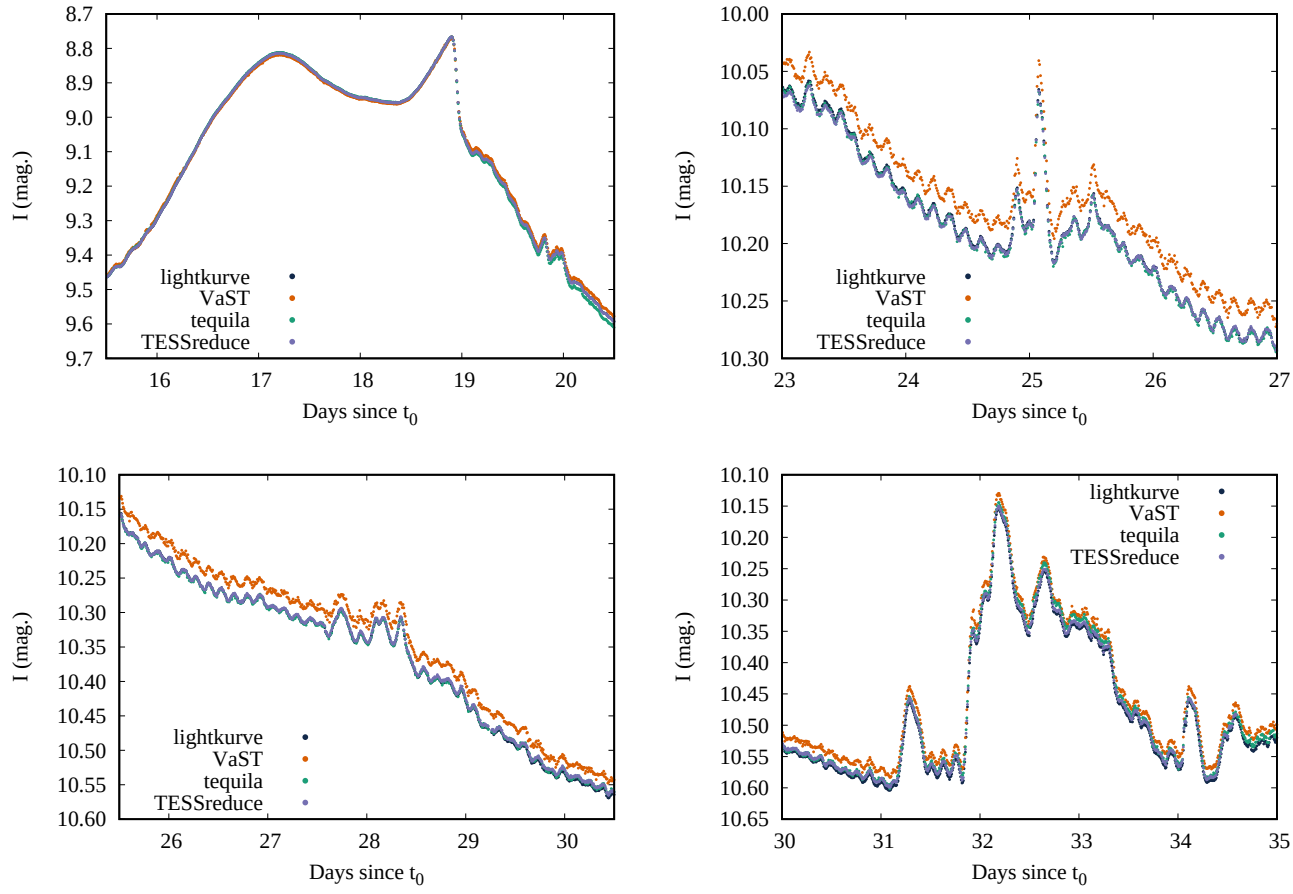

Figure 3. The details of the *TESS* lightcurve of V606 Vul showing "mini-flares" superimposed on the periodic oscillations pattern and the long-term trends. As in Figure 2, the color coding represents the lightcurves constructed with four different photometry codes described in § 2.1.

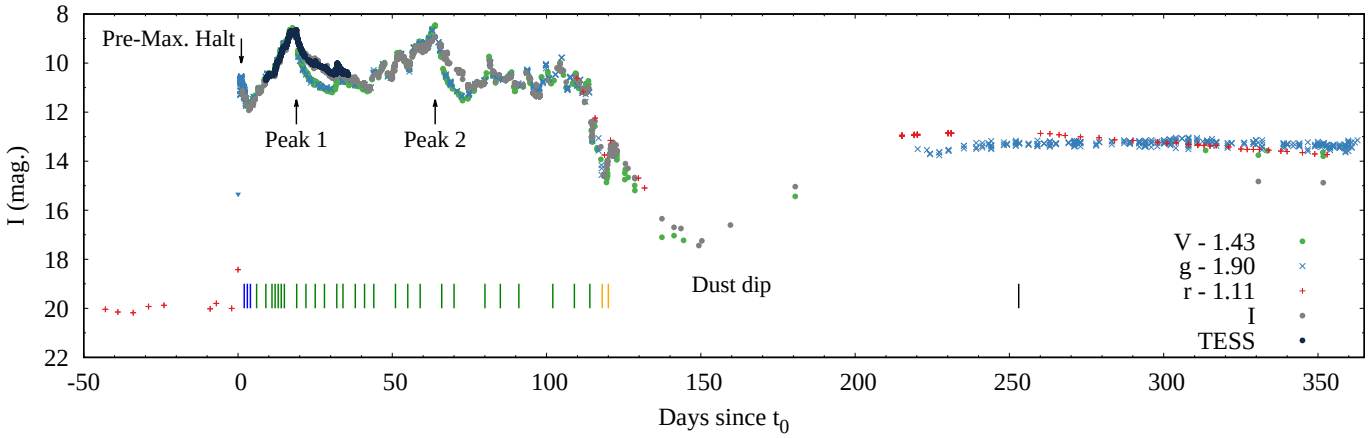

Figure 4. The lightcurve of V606 Vul covering the first year of eruption. The VI photometry is from the AAVSO and ANS, g-band observations are by ASAS-SN and Evryscope, r-band photometry is from ZTF. The offsets between the I-band and the gVr lightcurves are applied for visualization. The band-to-band offsets were determined using observations from the first 120 days of eruption, following the procedure outlined in § 2.2 for correcting offsets between observers within one band. The arrows in the plot mark the two prominent peaks and pre-maximum halt discussed in the text. The vertical lines mark the times of spectroscopic observations with their color (corresponding to Figure 5) reflecting the phase of nova spectral evolution (see § 2.3 and Aydi et al. 2024).

Gal-Yam et al. 2008 and Yuan & Akerlof 2008) and does not involve a search for an optimal convolution kernel that would match seeing of the reference image to that of the science image (Becker et al. 2012; Bramich et al. 2016). The algorithm ignores variations of the PSF and photometric scale (due to imperfect flat-fielding) across an image. This works fine for relatively small 127×127 pix cutouts from *TESS* FFIs, but would be a concern for wide-field images (Tomaney & Crotts 1996; Alard 2000; Bramich et al. 2013; Hu et al. 2022). Convolving the input FFIs with a Gaussian kernel having the standard deviation $\sigma = 2$ pix improves image subtraction results mitigating the effects of the undersampled PSF (Vallely et al. 2021).

The difference images are combined into a LIGHTKURVE target pixel file object. We use the 3×3 pix square aperture to extract photometry of V606 Vul from the difference images. The background-subtracted flux extracted from the reference image is added to the difference flux values. As the reference image includes the nova, care must be taken when converting the reference-image-flux-padded differential fluxes to magnitudes. We add a constant value to the differential fluxes before converting them to magnitudes. The constant value is chosen to match the peak-to-peak amplitude of the differential magnitude lightcurve to that of the aperture photometry lightcurve.

2.1.6. *Difference image analysis with* TESSREDUCE

TESSREDUCE (Ridden-Harper et al. 2021) uses TESSCUT to create LIGHTKURVE target pixel file objects from FFI cutouts. TESSREDUCE takes great care modeling background as the residual background variations are the dominant source of uncertainty in *TESS* photometry of faint objects. The background estimation procedure includes magnitude-dependent masking of known sources followed by 2D smooth background modeling and a special treatment of the vertical straps reflecting light from the back of the CCD (see fig. 3 of Ridden-Harper et al. 2021 and fig. 1 of Vallely et al. 2021). The sub-pixel shifts between the images in the x and y directions are determined from positions of stars measured with `photutils.detection.DAOStarFinder` (implementing the algorithm of Stetson 1987), smoothed in time (see fig. 4 of Ridden-Harper et al. 2021) and applied using `scipy.ndimage.shift` (spline interpolation). In contrast with TEQUILA_SHOTS, TESSREDUCE does not perform kernel matching as it relies on the stability of *TESS* PSF for a given region of the sky while observing one sector. Allowing only for shift and not rotation/scaling between the images and avoiding the image convolution step dramatically speed up computations. The default 3×3 pix square aperture centered on V606 Vul position was used for measurements, same as in § 2.1.3 and 2.1.5.

2.2. *Ground-based photometry*

The eruption of V606 Vul was closely followed by multiple observers sharing their data via the American Association of Variable Star Observers' (AAVSO) International Database (Kloppenborg 2022). After a visual inspection

of the lightcurve that resulted in rejection of a few outlier points, we were left with 6194 I-band and 1120 V-band measurements collected by 11 and 34 observers, respectively.

A common feature of heterogeneous photometric datasets is the presence of magnitude offsets between the individual observers. These offsets result from different filter-camera combinations producing slightly different spectral response and the different (sets of) comparison stars used by the observers. Observing in multiple filters quasi-simultaneously and performing transformation to a standard photometric system can reduce offsets (e.g., Budding & Demircan 2007; Boyd 2012), but is not always practical. We determine and compensate magnitude zero-point offsets between the observers by applying the following procedure independently to the I and V-band lightcurves:

1. Taking the lightcurve of the observer who contributed the most observations in this band as the reference (assume the offset is 0.0).

2. For the second most well-populated lightcurve try a range of offsets and pick the one that maximizes the value of the smoothness parameter $1/\eta$ defined in equation (1).

3. After applying the offset to the second most populated lightcurve, the same procedure is repeated to the third most-populated lightcurve and so on until all lightcurves from the individual observers are corrected.

The eruption of V606 Vul was also followed photometrically in $BVRI$ bands by the ANS Collaboration (Munari et al. 2012; Munari & Moretti 2012). All ANS observations are transformed from the local instantaneous photometric system to the standard Landolt (1992) one via solving the transformation color equations on each frame against a local photometric sequence extracted from APASS DR8 (Henden & Munari 2014); the sequence remain fixed for the all observing campaign and it is the same for all participating observer. As the ANS data are color-transformed, we use them without applying the inter-observer offset correction used for the AAVSO data.

We augmented the AAVSO and ANS I and V-band monitoring with data from three wide-fields surveys: g-band photometry from Evryscope (Law et al. 2014) and the All-Sky Automated Survey for Supernovae (ASAS-SN Shappee et al. 2014; Kochanek et al. 2017) combined with r-band photometry from the Zwicky Transient Facility (ZTF Masci et al. 2019) Public Data Release 13 accessed via the SNAD VIEWER (Malanchev et al. 2023). The ZTF lightcurve includes pre-eruption detections displaying a 0.3 mag scatter around the mean magnitude of $r = 21.2$ and the high point at $r = 19.53 \pm 0.08$ at $t_0 = HJD(\mathrm{UTC})\,2459410.88417$ (2021-07-15.38417; 1.1 days before the eruption discovery). In the following, we use t_0 as the eruption start time. The latest pre-eruption ZTF measurement is at $r = 21.11 \pm 0.18$ on $t_0 - 2.0$ days. The overall lightcurve of the eruption that combines the ground-based and TESS observations is presented in Figure 4. The TESS magnitude zero-point was shifted to match that of the AAVSO I-band lightcurve.

2.3. *Spectroscopic observations*

A set of low- and medium-resolution spectra of V606 Vul were obtained with the 2.5-m SAI Moscow State University telescope, 1.22-m Asiago, 4.1-m SOAR, and the 0.35-m telescope at Kolonica Saddle participating in the Astronomical Ring for Amateur Spectroscopy (ARAS; Teyssier 2019).

The 2.5-m SAI telescope observations where obtained using the Transient Double-beam Spectrograph (Potanin et al. 2020; Dodin et al. 2020) having the resolution R = 1300–2400 for the blue and red arms of the spectrograph that together cover the 3530–7420 Å range. V606 Vul was observed with the 1.22-m Asiago equipped with the Boller & Chivens spectrograph. The spectra were reduced as described by Zwitter & Munari (2000). V606 Vul was also observed using the Goodman spectrograph (Clemens et al. 2004), mounted on the 4.1-m Southern Astrophysical Research (SOAR) telescope located on Cerro Pachón, Chile. The spectra were obtained using the 400 l/mm grating, providing a resolving power R $\approx$ 1000, covering a range of 3800–7500 Å. The spectra were reduced and optimally extracted using the APALL package in IRAF (Tody 1986). We also made used of publicly available data from the Astronomical Ring for Access to Spectroscopy (ARAS; Teyssier 2019), specifically the low-resolution R $\approx$ 1000 spectra obtained at the Astronomical Observatory at Kolonica Saddle using the 0.35-m Schmidt-Cassegrain telescope equipped with Shelyak LISA spectrograph. Usually 5×1200 s exposures were used to construct a spectrum. The data reduction was performed using INTEGRATED SPECTROGRAPHIC INNOVATIVE SOFTWARE (ISIS) software. Wavelength calibration was done using an internal neon lamp and standard star (method implemented in ISIS). For instrumental response determination the same standard star was used.

The spectroscopic evolution of V606 Vul derived from these observations is presented in Figure 5. The color coding in the figure corresponds to the phases of nova eruption identified by Aydi et al. (2024):

1. (blue) The pre-maximum spectra dominated by P Cygni profiles of Balmer, He, and N.
2. (green) The near-peak spectra dominated by P Cygni profiles or emission lines of Balmer and Fe II.
3. (orange) The post-peak spectra again dominated by high-excitation lines of He and N along with Balmer lines.
4. (black) The nebular phase spectra are dominated by forbidden emission lines of O and Fe.

Figure 6 is a zoom-in on the H_β line highlighting the evolution of its profile.

3. RESULTS

3.1. *Comparison of* TESS *photometry methods*

The results produced by all the tested photometry codes are quite similar (Figures 2 and 3). The VaST lightcurve has a higher scatter because it re-centers the aperture on each image. Therefore, the VaST lightcurve is useful in this study mostly for quality assurance: to build confidence that the *TESS*-specific analysis methods do not introduce any unexpected systematics in the lightcurve. The remaining differences between the codes may be attributed to the different apertures used and the differences in the background estimations. For the following analysis we adopt the background-subtracted simple aperture lightcurve extracted with LIGHTKURVE.

3.2. *The lightcurve of V606 Vul*

The lightcurve of V606 Vul combining the ground-based and *TESS* photometry is presented in Figure 4. The eruption of V606 Vul starts with an elevated ZTF data point at t_0 1.6 magnitudes above the average quiescent level ($r = 21.18$) that is followed by a fast rise by 9.5 magnitudes in about 25 hours ($t_0 + 1.06$; the first peak time is constrained thanks to Evryscope photometry), at which point the eruption was discovered ($t_0 + 1.09$ d; 26 hours), shortly after passing the pre-maximum halt.

The pre-maximum halt is a feature observed in some novae that, according to Hillman et al. (2014), may signify the stage at which convection becomes ineffective in transporting energy to the surface of the expanding nova envelope and the radiation-driven mass loss begins. We argue that the initial rise of V606 Vul ends in a pre-maximum halt rather than a normal nova peak as the spectra obtained shortly after discovery are typical for a nova that has not reached its maximum yet (Figure 5).

The early AAVSO data show a decline from the pre-maximum halt by about 1 mag that around $t_0 + 3.5$ d turns over to a rise and the nova slowly climbs to its first peak (referred here as "Peak 1") of $I = 8.64$ at $t_0 + 18.901$ d (the sharp peak on top of the broader peak covered by *TESS* photometry that spans the time range form $t_0 + 9.1$ to $t_0 + 35.7$ d). The first peak is followed by an about equally-high ($I = 8.47$ color-transformed from $V = 9.90$) second peak ("Peak 2" in Figure 4) at $t_0 + 63.868$ d. The second peak is brighter than the first peak in V band, but not in I band where the actual measurements in this band peak around $I = 8.9$. After declining from the second peak the nova varies around a nearly-constant level of brightness until $t_0 + 114$ d, at which point a sharp decline starts that can be attributed to the formation of dust in the nova envelope. The dust clears around $t_0 + 200$ d at which point the nova is at $g \sim 15.4$ ($r \sim 14$) and displays a very slow decline by about 0.00525 mag/day (corresponding $t_{2\ g\ \mathrm{tail}} = 381$ d) in g (0.00927 mag/day corresponding to $t_{2\ r\ \mathrm{tail}} = 216$ d in r).

The lightcurve in bluer filters g and V does not follow exactly the lightcurve at the redder I and *TESS* bands (Figure 4). The notable deviations appear following the first and second peaks where the decline from the peak in I is notably slower than in g and V bands (the nova becomes redder after the peak). Similar color changes were observed in the flaring slow novae LMCN 2017-11a Aydi et al. (2019) and V1405 Cas (Valisa et al. 2023). It may be related to the "reddening pulse" phenomenon described by van den Bergh & Younger (1987) or increase of emission line flux (such as O I 7773Å and 8446Å) relative to continuum.

Taking the formal approach to the nova rate-of-decline determination we use the AAVSO data to measure that it took $t_2 = 3$ d ($t_3 = 9$ d) to decline by 2 mag (3 mag) form the maximum V-band brightness (reached during Peak 2). This, however, characterizes the rate of development of the individual major flare rather than the overall decline rate of the nova that is much slower.

Visual inspection of the *TESS* lightcurve (Figures 2 and 3) reveals three distinct variability patterns:

1. The *overall rise and decline* of the lightcurve at an uneven rate. The amplitude of the overall variations is 2 mag during the time interval covered by *TESS* observations (§ 2.1.1).

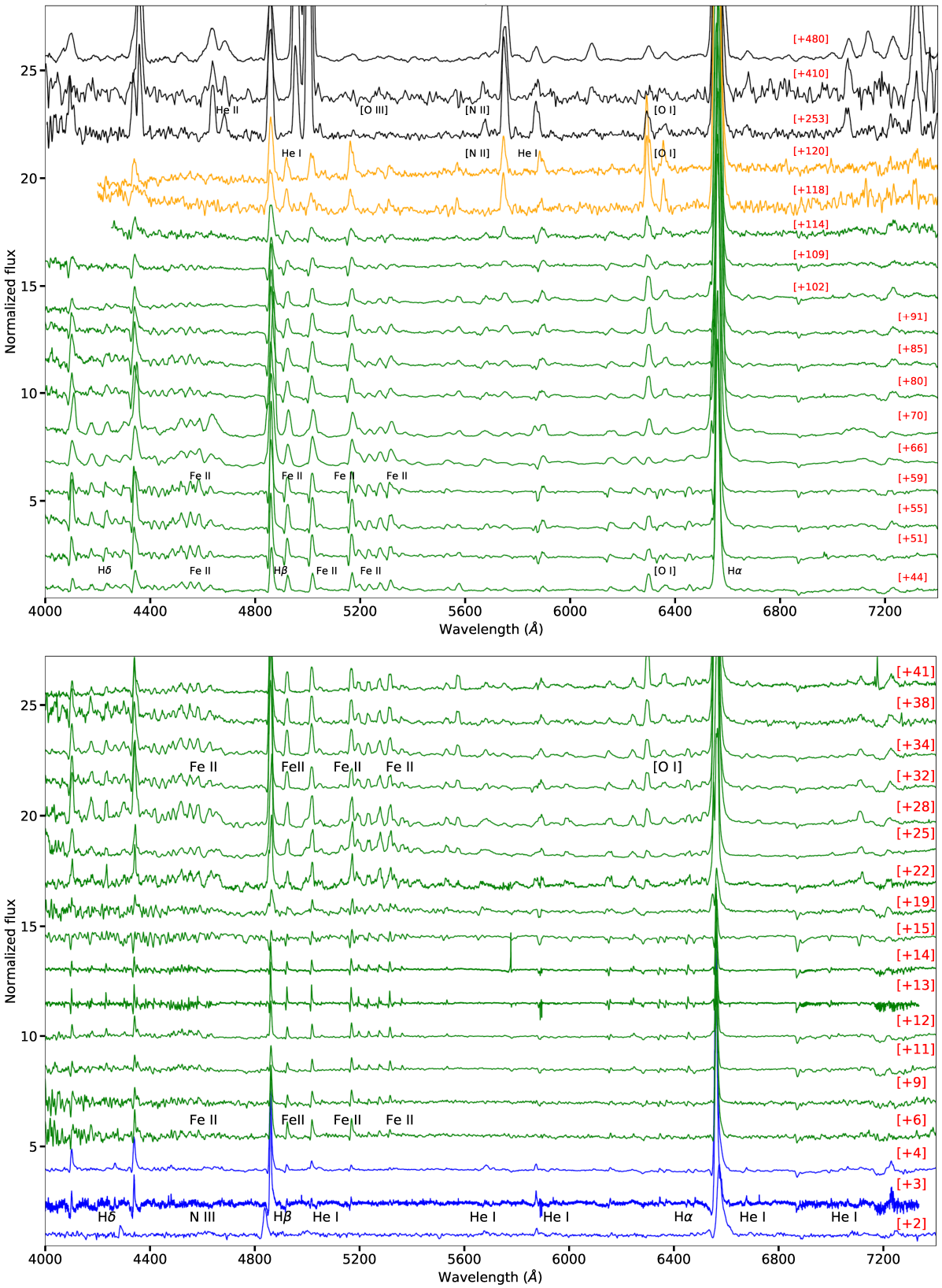

Figure 5. Spectral evolution of V606 Vul. The numbers in the brackets indicate the number of days past t_0. The color coding corresponds to the phases of nova eruption identified by Aydi et al. (2024), see also § 2.3: (blue) pre-maximum, (green) near-peak, (orange) post-peak, (black) nebular phase.

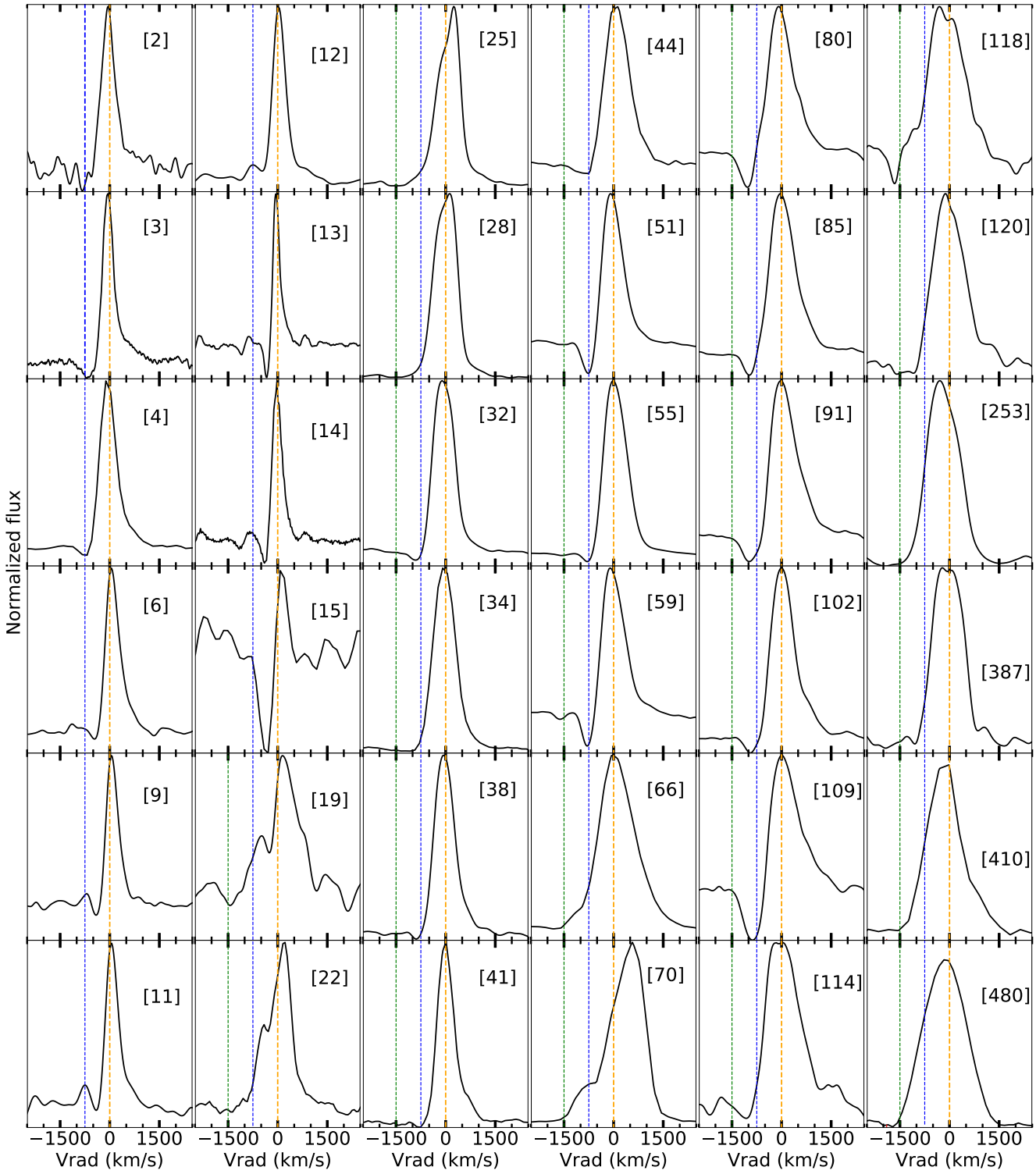

Figure 6. The H_β line profile evolution over the course of the nova eruption. The numbers between brackets are days past t_0. The orange, blue, and green dashed lines represent $v_{\rm rad} = 0, -750,$ and $-1500\,{\rm km\,s^{-1}}$, respectively.

2. A few sets of distinct *mini-flares* are visible during both the rising and declining parts of the overall lightcurve. The four panels of Figure 3 show the variety of shapes of mini-flares. The mini-flares have amplitudes up to 0.5 mag and rise and fall on timescales from ~ 0.1 d (orbital period?) to ~ 1.5 d. Multiple flares tend to cluster together interleaved by intervals of smooth flare-less variations.

3. Low-amplitude (~ 0.01 mag peak-to-peak) periodic variations visible both on the rising and declining branches of the lightcurve in the magnitude range $I = 9.4$ to 10.7. They become invisible when the nova approaches its $I = 8.6$ peak (Peak 1). It is hard to tell if the mini-flares interrupt the periodic variations as the mini-flares clearly have structure on timescales comparable to the period and their intrinsic (undistorted by the periodic modulation) shape is unknown.

3.3. *Periodicity search*

We used the VaST interactive lightcurve plotting tool to manually exclude the episodes of flaring activity and times of rapid magnitude variations and subtract a piecewise linear function (plotted as a series of green lines in Figure 2) that approximates long-term variations from the *TESS* lightcurve of V606 Vul. The power spectrum (Deeming 1975; VanderPlas 2018) constructed over this *detrended* lightcurve is presented in Figure 7. We also plot the spectral window (see Deeming 1975; Scargle 1982; VanderPlas 2018; Goyal et al. 2022). The spectral window peak is normalized to the power spectrum peak for display purposes. The power spectrum is in units of squared amplitude (half of the peak-to-peak amplitude), consistent with the definition used by Max-Moerbeck et al. (2014a). The power spectrum of the detrended lightcurve has a clear peak corresponding to the following light elements:

$$\mathrm{HJD(TDB)}_{\max} = 2459441.75784 + 0.12771 \times E \tag{2}$$

We conservatively estimate the uncertainty of the period, P, from the duration of the lightcurve, JD_{range} as discussed in the Appendix of Sokolovsky et al. (2022b):

$$P_{\mathrm{err}} = 0.5P^2/\mathrm{JD}_{\mathrm{range}} = 0.00038\,d = 33\,s. \tag{3}$$

The total duration of the detrended lightcurve used for period search is 21 d (less than the full duration of Sector 41) as it excludes the series of mini-flares starting around $t_0 + 31$ d as well as the first 0.5 d of the *TESS* lightcurve that are not well approximated by a linear function. Only the sections of the lightcurve for which the trend-fitting lines are displayed in Figure 2 were used to derive the period. We repeated the analysis using the full Sector 41 lightcurve (not only the times where the periodic modulation is visible) smoothed using the Savitzky & Golay (1964) filter with outlier point clipping at 3σ level. This approach has minimal human input (apart from selecting the filtering parameters) and results in a noisier lightcurve, yet the periodic modulation is still detected. This confirms that the detection of the periodic modulation does not depend on the choice of the detrending algorithm and time intervals. The details of this alternative analysis are available online[1].

The periodicity presented in Figure 7 is highly significant with the probability of chance occurrence of $\ll 10^{-5}$ estimated from bootstrapping (lightcurve shuffling; see § 7.4.2.3 of VanderPlas 2018). We checked that this period is also found with the Lomb-Scargle periodogram (analytically computed false alarm probability $\ll 10^{-5}$; Lomb 1976; Scargle 1982; VanderPlas 2018), the Lafler & Kinman (1965) string-length method (agnostic to the shape of the phased lightcurve) and the Schwarzenberg-Czerny (1996) method based on the analysis of variance statistic fitting of periodic complex orthogonal polynomials (using 4 harmonics expansion to account for the possible non-sine-wave-like shape of the phased lightcurve).

While in general identification of a periodic signal in the presence of red noise (§ 3.4) is a complex problem (Pont et al. 2006; Vaughan 2010; Vaughan et al. 2016; Krishnan et al. 2021), the periodic signal in the *TESS* lightcurve of V606 Vul is so strong and persistent that it cannot realistically be expected to arise from noise. The periodic modulation is clearly visible in the lightcurve before detrending (Figure 3) and the consistent modulation frequency is found from periodicity search in non-overlapping sub-sections of the lightcurve ("before" and "after Peak 1" lightcurves in the left panel of Figure 7). The longest lightcurve section uninterrupted by mini-flares (indicated with green lines around $t_0 + 30$ d in Figure 2) includes 18 complete cycles of variation. All these considerations point to the periodicity being a real feature of the source rather than an artifact of detrending a red-noise dominated lightcurve.

The phase of the periodic variations is not interrupted by mini-flares nor the long period of high brightness (Peak 1) when the periodic variations temporarily disappear. The phase stability of the variations, illustrated by Figure 7,

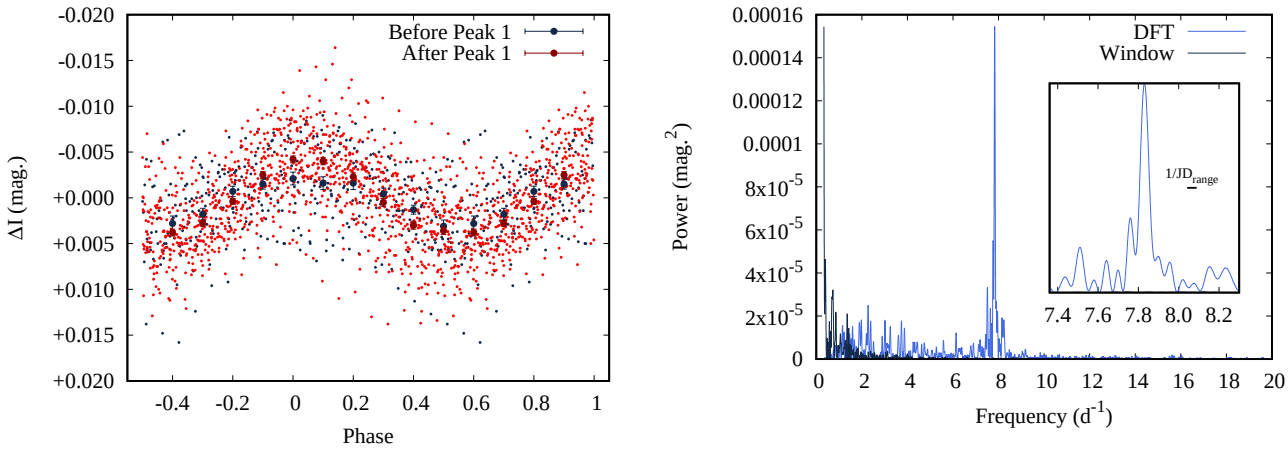

Figure 7. The detrended *TESS* lightcurve of V606 Vul (left panel) phased with the light elements (2) and the corresponding power spectrum and spectral window (right panel). Only the times overlapping with lines plotted in Figure 2 were used in the period analysis. The color in the phased lightcurve plot indicates measurements obtained before and after Peak 1 (the brightness maximum reached by V606 Vul during the *TESS* observations). The large markers indicate the mean magnitude in a 0.1-wide phase bin and the corresponding uncertainty of the mean. The insert in the power spectrum plot details the structure of the main peak with the Rayleigh resolution labeled $1/\mathrm{JD}_{\mathrm{range}}$ indicated by the horizontal bar placed at half the peak's magnitude.

suggest its relation to the orbital motion of the binary. Depending on the physical origin of the modulation, the orbital period may be equal to or twice as long as the observed photometric periodicity.

Schmidt (2021a) reports the detection of what might be the same periodic signal in ground-based photometry of V606 Vul obtained by the author over a time span of 57 d. However, the period derived by Schmidt (2021a) is 8 min longer than the one we derived from *TESS* photometry. **The origin of this difference is unclear. It could be related to uncertainties in lightcurve detrending.** We highlight the tentative detection of the periodic signal by Schmidt (2021a) to point out the prospects of searching for similar periodic signals in other novae using ground-based photometry. A reliable detection of such signal would probably require a dedicated multi-site observing campaign and careful lightcurve detrending, but appears technically feasible.

3.4. *Power Spectrum*

The power spectrum is also useful for characterizing non-periodic variability where the power is spread among a range of frequencies rather than being concentrated in a narrow peak (as is the case of a periodic signal). The power spectrum analysis is often applied to X-ray binaries and active galactic nuclei (e.g., Vaughan et al. 2003; González-Martín & Vaughan 2012; Smith et al. 2018a). Three main types of features may generally be found in a power spectrum:

1. one or more narrow peaks corresponding to strictly periodic variations,
2. a broad peak corresponding to quasi-periodic oscillations (that appear and disappear at different frequencies around some characteristic frequency),
3. stochastic variations continuum that often can be approximated with a power-law.

A change in the power spectrum continuum slope at a certain frequency may indicate a time and hence a length scale important in a studied astrophysical system (Revnivtsev et al. 2009; Scaringi et al. 2015; Suleimanov et al. 2019; Burke et al. 2021; Mönkkönen et al. 2022). To our knowledge, what we describe below is the first attempt to characterize the power spectrum slope of irregular variations near a peak of a nova eruption.

We use the Deeming (1975) definition of discrete Fourier transform (DFT) – the same one we used for periodicity search in § 3.3 – to construct the power spectrum from the *non-detrended TESS* Sector 41 lightcurve of V606 Vul. Figure 8 presents the power spectrum in the log-log scale. The differences with the right panel of Figure 7 are that the *TESS* lightcurve was taken in flux (rather than magnitude) units and no detrending was applied before computing the power spectrum. Without detrending aimed at suppressing low-frequency variations, the periodic

variation peak (marked with an arrow in Figure 8) is barely visible among non-periodic variations. We characterize the continuum slope by least-square fitting a line to the binned power spectrum in the log-log scale – a commonly used (e.g., Wehrle et al. 2013; Otero-Santos et al. 2020; Raiteri et al. 2021), if not statistically optimal procedure. We exclude the two low-frequency points and naively assign the same weight for the remaining points before performing the linear fit (while Uttley et al. 2002 suggested a better way to assign error bars to the binned power spectrum based on simulations; see also Smith et al. 2018b). We find that the power of non-periodic variations in V606 Vul declines inversely proportionally to the frequency squared – the "random walk" red noise. Apart from the periodic variations peak, there are no obvious deviations from the power-law power spectrum density within the frequency range probed by the *TESS* Sector 41 lightcurve.

For comparison, we briefly summarize what power spectrum continuum shapes are found in various classes of sources. Accreting white dwarfs often display "flicker noise" (pink noise) power spectra with the slope of $\alpha \simeq -1$ (Baptista & Bortoletto 2008; Dobrotka et al. 2012; Baptista et al. 2016; Bruch 2022), while the earlier studies pointed to $\alpha \simeq -2$ (Elsworth & James 1986; Bruch 1992). The lightcurves of accretion-disk-dominated AGNs are often modeled as "damped random walk" (also known as an Ornstein-Uhlenbeck process or a continuous-time autoregressive model of the first order) with the spectral slope fixed to $\alpha_{\rm high} = -2$ well above and $\alpha_{\rm high} = 0$ well below some break frequency (MacLeod et al. 2010; Burke et al. 2020; Stone et al. 2022). Scaringi et al. (2015) argue that a broken power-law shape of a spectrum is a common feature of all accreting systems, from cataclysmic variables and young stellar objects to stellar-mass and supermassive black holes. In jet-dominated AGNs (blazars) the damping timescale is often not constrained (for counterexamples see Sobolewska et al. 2014) and the power spectrum is consistent with a single power-law, but different slopes are reported as typical at different bands: $\alpha_{\rm GeV} \simeq -1.5$ (Max-Moerbeck et al. 2014b; Tarnopolski et al. 2020; Bhatta & Dhital 2020), $\alpha_{\rm optical} \simeq -2$ (Burke et al. 2021; Pininti et al. 2023), $\alpha_{\rm radio} \simeq -2$ (Max-Moerbeck et al. 2014b; Park & Trippe 2017). Goyal et al. (2022) suggested that the power spectrum slope is flatter for inverse Compton than synchrotron emission of the same blazar jet. In summary, comparison of the observed power spectrum slope with the values reported in the literature does not allow one to prefer accretion over ejection as the driver of stochastic variability. We note that the power-law power spectrum may be produced by a superposition of discreet flares (Terrell 1972; Burderi et al. 1993) as well as a continuous change in parameters of the emitting region (Lyubarskii 1997), so it cannot discriminate between these scenarios.

3.5. *Structure Function*

Irregular variations may also be characterized in time (rather than frequency) domain with the structure function, SF, that represents the variability amplitude as a function of the time lag between brightness measurements. The SF is often applied to the analysis of AGN lightcurves from X-ray to radio bands (e.g., Collier & Peterson 2001; Schmidt et al. 2010; Caplar et al. 2017). According to MacLeod et al. (2010), the SF may be less sensitive to aliasing and other time-sampling problems than the power spectrum.

We compute the SF by taking the mean squared difference between the lightcurve values $S(t)$ separated by a time lag Δt following the simple definition from Hughes et al. (1992):

$$\mathrm{SF}(\Delta t) = \langle [S(t) - S(t + \Delta t)]^2 \rangle, \tag{4}$$

see also Kozłowski (2016) and Graham et al. (2014) for a detailed discussion and alternative definitions of SF. Emmanoulopoulos et al. (2010) criticize the practice of using SF to characterize irregular variability favoring PSD reconstruction instead (§ 3.4).

Figure 9 presents the $\sqrt{\mathrm{SF}}$ computed from *TESS* Sector 41 lightcurve and the first 100 days of AAVSO and ANS V and I band observations of V606 Vul (before the dust dip). The SF is computed using the magnitude ($S(t_i) = m_i$) rather than flux lightcurve to simplify interpretation and comparison with Figures 2 and 4.

The *TESS* and AAVSO+ANS SFs display a change of slope around $\Delta t_{\rm var} = 8$ d which we cautiously interpret as the longest timescale of flaring activity in V606 Vul (the variability pattern corresponding to the two peaks and the flare-like activity surrounding them). However, Emmanoulopoulos et al. (2010) note that spurious breaks can be found in SF at timescales ~ 0.1 of the lightcurve length. At longer timescale ($\Delta t \gg \Delta t_{\rm var}$), the SF is not well constrained due to the finite length of the *TESS* lightcurve, so the decline of the *TESS* SF at $\Delta t > 10$ d is not real, as seen from comparison with the AAVSO+ANS data. At $\Delta t < \Delta t_{\rm var}$ the *TESS* SF looks like as simple power-law (corresponding to a straight line when plotted in the log-log scale) that goes all the way to the shortest timescales that can be probed with *TESS* FFIs. The absence of another turnover at short timescales that would correspond to the noise level

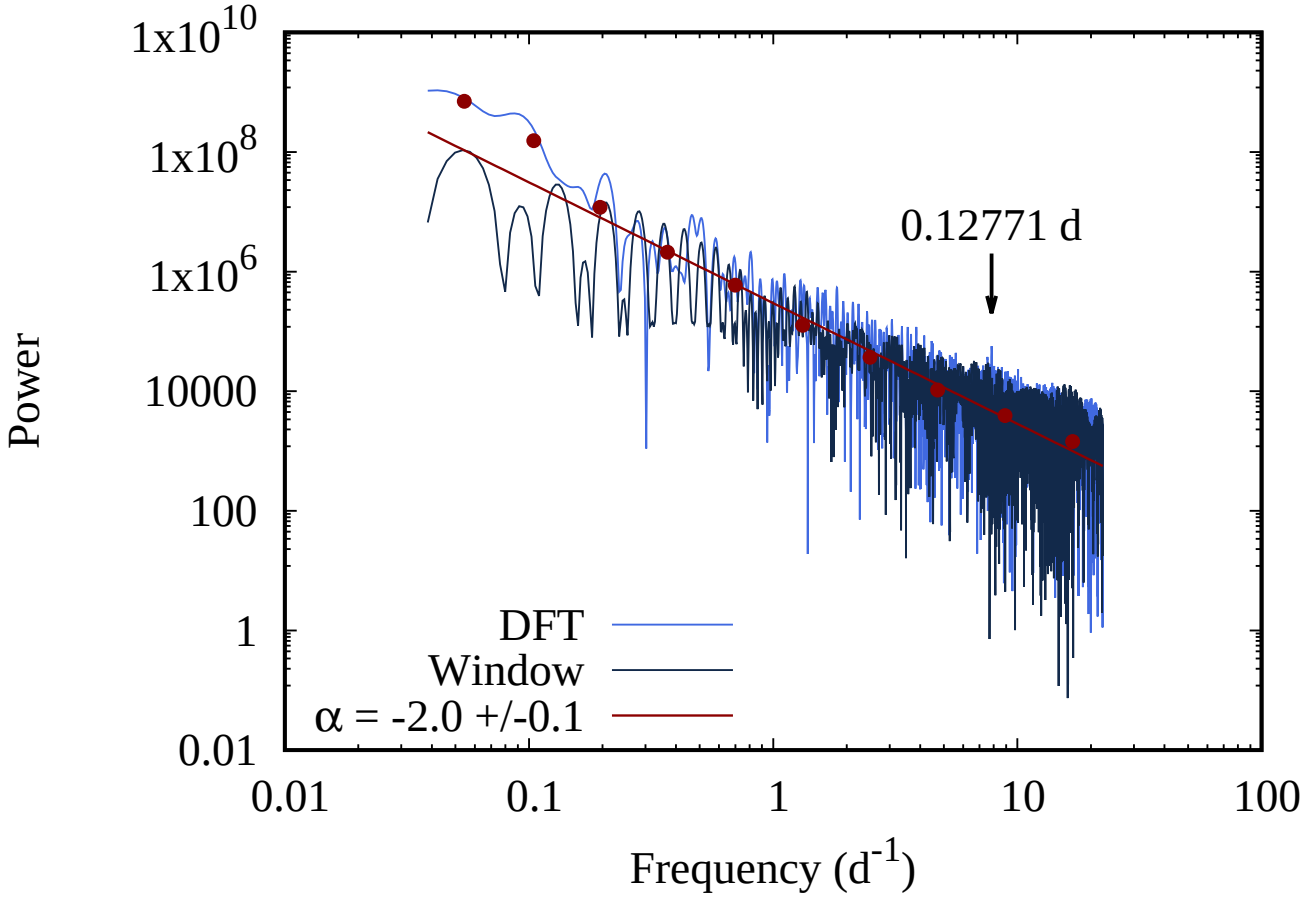

Figure 8. The power spectrum (DFT) constructed from the non-detrended *TESS* lightcurve of V606 Vul and the corresponding spectral window. The power is plotted in arbitrary units and the spectral window is shifted from the DFT for clarity. The red points show the binned power spectrum and the red line is the power-law with the slope $\alpha = 2.0 \pm 0.1$ approximating it. The power-law fit excludes the two low-frequency bins likely affected by red leak (e.g., Papadakis & Lawrence 1993; Uttley et al. 2002). If they are included, the best-fit $\alpha = 2.3 \pm 0.1$.

(see fig. 1 of Hughes et al. 1992) indicates that significant brightness variations in V606 Vul are detected down to the shortest timescales probed by *TESS* FFIs, with a typical variability amplitude of about $\sigma = \sqrt{SF/2} = 0.015$ mag over a timescale of an hour. The V and I band SFs produced from ground-based observations lay above the *TESS* SF and are considerably more noisy as they incorporate higher photometric errors and imperfectly corrected zero-point offsets between the observers. The periodic signal discussed in § 3.3 that has even smaller amplitude is not visible with the binning used in Figure 9.

3.6. *Evolution of the optical spectrum*

During the rise to peak, the spectra of V606 Vul, are dominated by P Cygni lines of Balmer, He I, N II, and N III (see Figures 5 for the complete spectral evolution of V606 Vul). As the nova climbs to peak, the He and N lines weaken, while Fe II P Cygni lines emerge, particularly of the (42), (48), and (49) multiplet. These lines remain the strongest lines in the spectrum until around 115 days past t_0, when the nova starts declining rapidly. At this stage strong lines of He I, [N II], and [O I] become prominent. This evolution of spectral features going from He/N to Fe II and then He/N is described in details in Aydi et al. (2024). After day 250, the spectra show strong forbidden lines of O II, O III, N II, and permitted lines of N II and He II, signaling that the nova has entered the nebular phase.

Throughout the evolution of the nova, the line profiles also show significant changes, particularly associated with the appearance of new peaks in the optical light curve. The P Cygni absorption troughs are characterized by velocities of a few hundreds km s^{-1} (300 to 500 km s^{-1}). As the nova declines from the first peak, the line profiles shift from

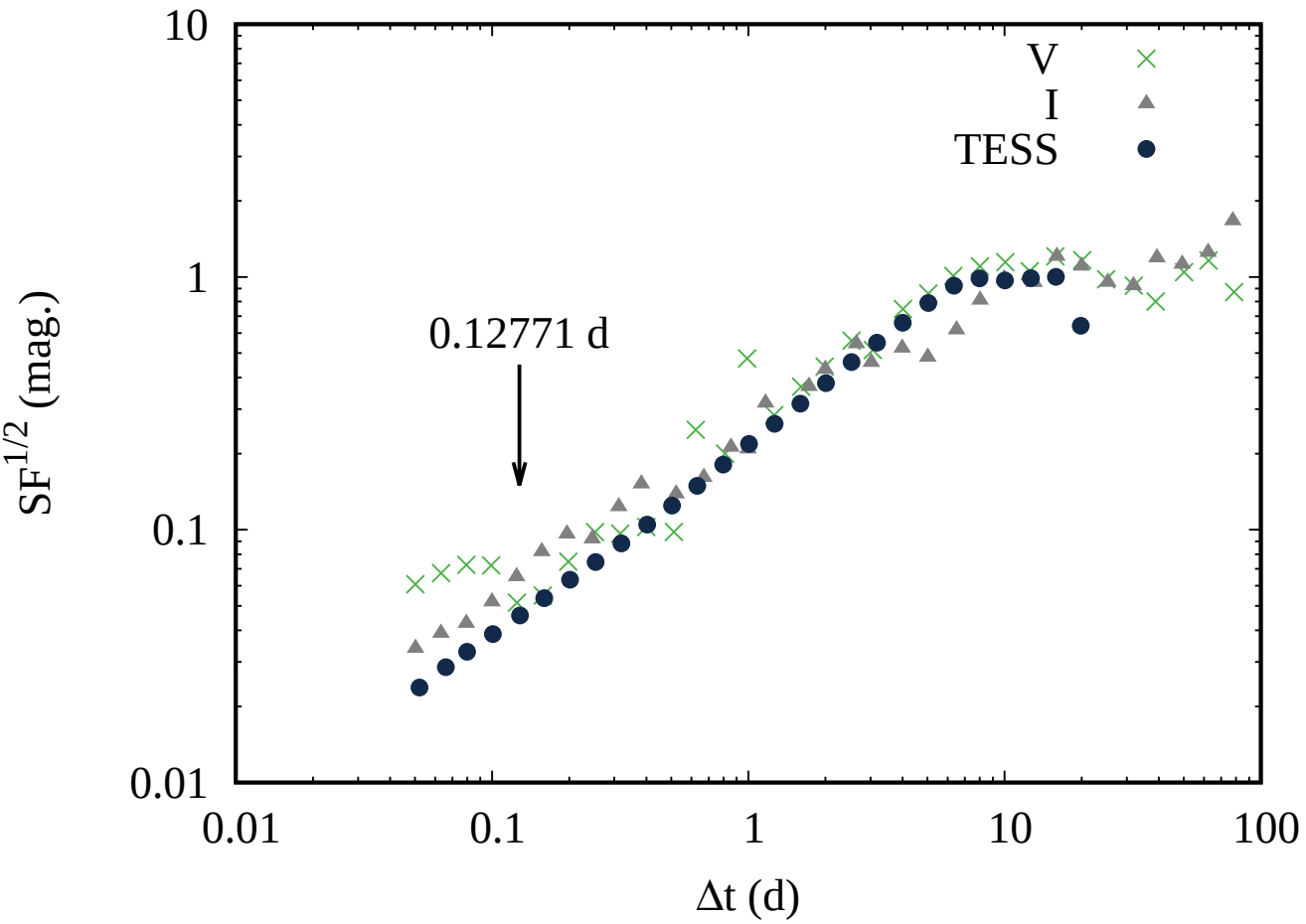

Figure 9. The square root of the structure function as defined by Hughes et al. (1992) computed from *TESS* Sector 41 lightcurve and the first 100 days of AAVSO and ANS V and I band photometry of V606 Vul. The arrow marks the position of the periodic signal that cannot be distinguished in the SF plot due to the low amplitude of the signal.

P Cygni to mostly emissions, as the absorptions become shallower in comparison to the emissions. We also notice the emergence of broader emission lines with velocities of around 1500 km s^{-1}, while the P Cygni profiles are still superimposed on top of them. The presence of multiple velocity features in the spectra of novae has been discussed extensively in the literature in the context of multiple phases of mass-loss (e.g., Friedjung 1987, 2011; Tanaka et al. 2011a,b; Aydi et al. 2020a)

In Figure 6 we present the evolution of H$_\beta$, highlighting the significant changes in the line profiles and the multiple velocity features. As the nova rises again to the second major peak (day 50), the absorptions in the P Cygni lines become prominent again. Similar to the behavior after the first peak, the absorptions also fade as the nova declines from the second peak past-day 60.

Around day 80, coinciding with new smaller peaks (flares) in the visible light curve, H$_\beta$ line profiles show again absorption features but now at greater velocities (around 1000 km s^{-1} on day 80 and around 1700 km s^{-1} around day 118). Due to the low resolution of the available spectra it is challenging to disentangle the different absorption features and measure their velocities accurately. However, it is common to observe multiple absorption/emission features at a range of velocities in novae with multiple peaks (flares) in their light curve. These new spectral features have been observed to coincide with the appearance of and were associated with new phases of mass-loss or ejections (e.g., Tanaka et al. 2011a,b; Aydi et al. 2019, 2020b,a)

In summary, the spectral evolution of nova V606 Vul is complex, showing drastic changes coincident with changes in the brightness of the nova and is consistent with the complex spectral evolutions exhibited by other flaring novae. However, the presence of multiple absorption/emission features at distinct velocities in the spectra of nova V606 Vul

suggest that some of the flares in the light curve, particularly the major ones (Peak 1, Peak 2, and some of the smaller flares between days 80 and 120), are possibly caused by new episodes of mass-loss.

4. DISCUSSION

The *TESS* lightcurve of V606 Vul reveals two interesting features:

1. periodic variations that are present except when the system was within 1 mag of peak optical brightness;
2. mini-flares appearing at seemingly random times in a series of one or more and separated by quiescent times of apparently undisturbed periodic variations.

In this section we discuss how unusual these features are among the previously observed novae and consider their possible physical interpretation.

4.1. *Space-based photometry of novae: the few lightcurves with no diurnal gaps*

This study pioneers the use of *TESS* photometry in investigating nova eruptions. Previously, lightcurves of several Galactic novae were constructed from space-based optical observations. The advantages of space-based photometry include enhanced instrument stability and the ability to make continuous observations, unhindered by the Earth's day-night cycle (Weiss et al. 2021). This uninterrupted observation capacity enables the capture of variability on a 12–24 hour timescale, a challenging feat for ground-based observers.

The Solar Mass Ejection Imager on board the *Coriolis* satellite was used to construct lightcurves of 14 novae revealing a pre-maximum halt in six of them and fast apparently irregular variations near the peak of the slow recurrent nova T Pyx (Hounsell et al. 2010; Surina et al. 2014; Hounsell et al. 2016). The nova V5583 Sgr was observed with *STEREO*-A's outer Heliospheric Imager (HI-2) (Holdsworth et al. 2014). Another nova that erupted close to the ecliptic plane, V5589 Sgr was within the field of view of *STEREO*-B's inner Heliospheric Imager (HI-1) telescope (Eyres et al. 2017; Thompson 2017). These instruments designed to observe solar corona were not optimized for stellar photometry. As a result, the data analysis was complicated and noticeable discrepancies between different reductions of the same data (V5589 Sgr) and between the space-based and ground-based observations were reported, undermining overall confidence in the extracted lightcurves.

A substantial step forward was furnished by the chance observation of nova V906 Car by *BRITE-Toronto* – a member of the BRIght Target Explorer nanosatellite constellation dedicated to optical photometry of bright stars (Pablo et al. 2016). V906 Car displayed a series of distinct flares during a prolonged plateau near its peak brightness. Remarkably, the optical flares echoed $\sim$ 1 GeV γ-rays observed by *Fermi*-LAT (Atwood et al. 2009) revealing that shocks (accelerating the γ-ray emitting particles) are also responsible for the optical flares (likely resulting from reprocessed shock thermal X-ray emission; (Aydi et al. 2020b)).

Nova lightcurves were also constructed with ultraviolet telescopes starting with *OAO-2* observations of FH Ser (Gallagher & Code 1974). Multiple novae were monitored with *Swift*/UVOT (Page et al. 2022). As these observations required a dedicated satellite pointing to obtain each data point, the resulting cadence is often not superior to that of optical lightcurves obtained from the ground.

In summary, irregular variations near the peak brightness as well as isolated flares were reported in novae previously observed from space during eruption. No periodic variations near peak brightness were previously found with space-based photometry.

4.2. *Orbital period modulation in novae*

Periodic optical light variations apparently related to the binary orbital motion were observed from the ground during the decline phase in a number of fast novae. The very fast nova V838 Her (t_2 = 1–2 d Vanlandingham et al. 1996; Strope et al. 2010) started displaying eclipses when it was 7.5 mag below and 21 d after the peak (Kato 2023). V1674 Her, the fastest known classical nova with (t_2 = 1.1–1.2 d Quimby et al. 2021; Shugarov & Afonina 2021), started displaying orbital modulation just 4 days after (but already 4 mag below) the peak according to Patterson et al. (2022), while the analysis of Luna et al. (2024) suggest a later start of orbital modulation: after day 15. The recurrent nova U Sco (t_2 = 1.2–1.8 d; Schaefer 2010; Munari et al. 2010) started displaying eclipses about 14 days (and about 6 mag below) the peak after its 2010 eruption (Schaefer et al. 2010; Pagnotta et al. 2015). Another recurrent nova CI Aql (t_2 = 25 d Strope et al. 2010) showed sinusoidal modulations starting 40 d after (and **about 3.5 mag** below Schaefer

2010) the peak (Schaefer 2011) with no eclipses that were normally observed in this system (Mennickent & Honeycutt 1995), suggesting that the light source was larger than the binary system while displaying the sine-wave orbital modulation.

V959 Mon, the first nova discovered as a GeV transient near its solar conjunction and identified in optical 50 days later displayed orbital modulation dominated by irradiation of the secondary (one hump per orbit) with a contribution of ellipsoidal variability due to secondary filling its Roche lobe (two humps per orbit; Munari et al. 2013). The extremely slow nova V723 Cas, that displayed multiple peaks in its lightcurve, started displaying orbital modulation more than a year after (and 2 mag below) its peak brightness (Goranskij et al. 2000; Shugarov et al. 2005; Ochner et al. 2015). The orbital modulation in V723 Cas is also interpreted in terms of irradiation of the secondary.

Nova Cygni 1975 (V1500 Cyg; $t_2 = 2$ d Lance et al. 1988; Strope et al. 2010), a naked-eye nova that erupted in a polar-type magnetic cataclysmic binary, is also known for its periodic variations detected 4.5 mag below and ~ 10 days past the peak (Tempesti 1975). The periodic variations observed days after the eruption were associated with the spin of the magnetic white dwarf that somehow coupled with the expanding nova envelope (Stockman et al. 1988; Somers & Naylor 1999), while losing synchronization with the binary motion. At later epochs, the photometric variability of V1500 Cyg was dominated by the orbital modulation, thought to be dominated by irradiation of the secondary by the hot white dwarf (e.g., Schmidt et al. 1995; Harrison & Campbell 2016; Pavlenko et al. 2018).

Low-amplitude periodic modulation about 1–2 mag below and 3–4 months *before* the peak has been reported by Schmidt (2022) in an exceptionally slow and poorly observed nova PGIR22akgylf (De et al. 2022). Schmidt (2021b) reported orbital periodicity in the slow multi-peak nova V1391 Cas detected while the nova was within 2–3 magnitudes of its peak brightness. Schmidt (2021c) and Thomas et al. (2021) reported two inconsistent periods of orbital modulation in a multi-peak nova V1112 Per, from the published lightcurve it is unclear when this modulation might have appeared.

Orbital modulation well below the peak due to irradiation of the secondary is also reported for V1974 Cyg (De Young & Schmidt 1994), V407 Lup (Aydi et al. 2018), V392 Per (Munari et al. 2020; Murphy-Glaysher et al. 2022), and there is a number of old novae displaying eclipses including DQ Her (Zhang et al. 1995), BT Mon and others listed by Schaefer (2020). Schaefer (2022b) presents a comprehensive study of orbital periods in old novae, often relying on photometric modulation to derive a period (see also Schaefer 2021 and Fuentes-Morales et al. 2021).

Overall, photometric modulations at the orbital period are commonly found in novae, but usually when novae fade at least 2–4 mag below the peak brightness (in one to few t_2 times). The modulation is usually explained by the dominating irradiation effect, sometimes with additional contribution from eclipses, and ellipsoidal variations of the secondary – scenarios all requiring a direct view of the binary.

The observation of CI Aql (following its 2000 eruption) displaying sine-wave orbital modulation with eclipses appearing later is interpreted by Schaefer (2011) as "an emission region... substantially larger than the binary orbit and... transparent enough so that the inner regions can be seen (with the irradiation of the inner hemisphere on the companion providing the modulation with the orbital period)." It is interesting to note that among the listed examples the slow multi-peak novae V723 Cas, V1391 Cas and PGIR22akgylf that mostly resemble V606 Vul, are the ones displaying orbital modulation closer to the peak brightness compared to the fast novae with a single well-defined lightcurve peak.

The observed orbital period distribution of novae peaks between 3 and 4 hours (Tappert et al. 2013; Fuentes-Morales et al. 2021; Schaefer 2022b) and extends both toward longer and shorter periods. Theoretical predictions for nova orbital period distribution are discussed by Nelson et al. (2004); Townsley & Bildsten (2005); Chen et al. (2016); Hillman et al. (2020).

4.3. *The origin of periodic modulation in V606 Vul*

The conventional wisdom is that "novae before the transition phase (see § 4.5), including around the peak, cannot display any coherent periodicity because the opaque shell hides the inner binary"[2] (MacDonald 1980; Livio 1990). This conventional wisdom however is at odds with the *TESS* photometry presented in § 2.1 and § 3.3.

We consider the following scenarios for the origin of the orbital modulation in V606 Vul:

1. The envelope remains partly transparent, even close to the peak. This picture is an extreme version of **the eclipsing recurrent nova** CI Aql interpretation by Schaefer (2011) **(see his figure 8) discussed in § 4.2.**

[2] Brad Schaefer's comment on the VSX page of V2891 Cyg https://www.aavso.org/vsx/index.php?view=detail.top&oid=1498445

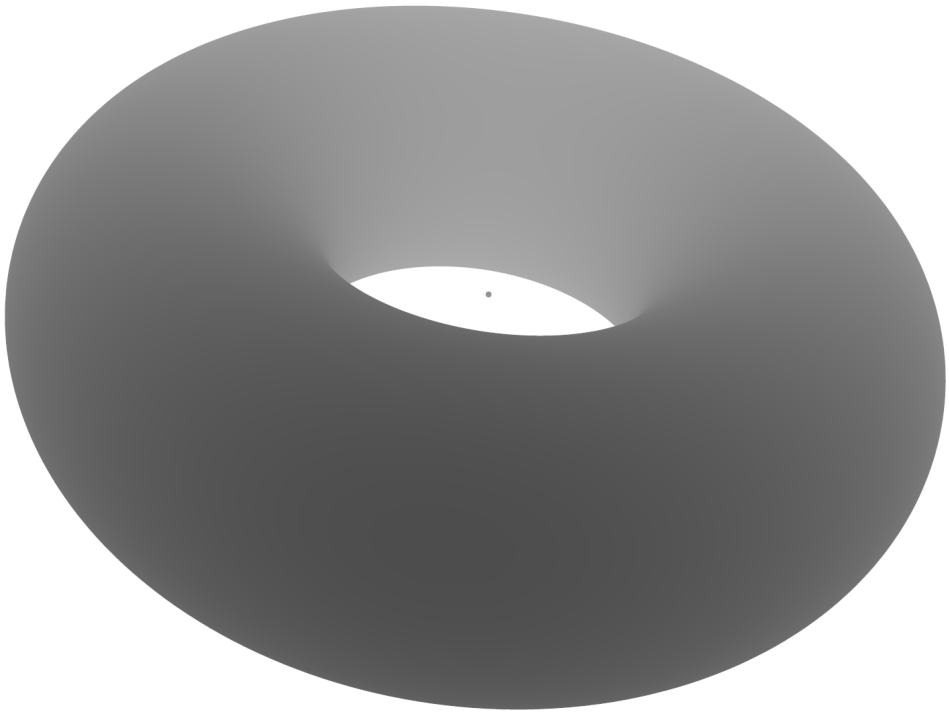

Figure 10. A sketch of an example ejecta geometry allowing direct view of the binary.

CI Aql displayed 0.16 mag modulation 40 days after and 3.5 mag below the peak of its eruption 2000. If the binary is still visible during the nova peak (it's the additional unmodulated light that gets 3.5 mag brighter), the same modulation in flux units would translate to a 0.006 mag amplitude in magnitude units – comparable to the amplitude of modulations we observe in V606 Vul (Figure 7). One possibility is that the nova ejecta (and the photosphere) might have a shape of a torus, allowing a direct view of the binary at low inclinations (Figure 10). The "direct view of the binary" scenario implies that as the nova envelope becomes more transparent and faint, the periodic modulation is expected to become more prominent. The problem with this scenario is that it is unclear if the binary itself can contribute as much as one percent of the total light near the peak brightness of a nova - the ejecta is likely to outshine the binary even if it's not obscuring it. **We note also that the early post-eruption modulation in CI Aql does not show eclipses that this system displays in quiescence, so the source of the modulated light during eruption might be relatively large. Also the polar hole geometry depicted in Figure 10 does not apply to CI Aql, as the eclipses imply that system is seen edge on, but in the case of V606 Vul could we be looking at a similar system through a polar hole?**

2. The emitting region might be larger than the binary and opaque, but instead have a gradient in temperature: the side of the envelope above the white dwarf might be slightly hotter (and brighter) than the side of the envelope above the secondary. The temperature gradient could be produced if there is a secondary source of heating located near or below the optical photosphere: such as internal shocks or binary frictional (drag) heating **(Kato & Hachisu 1994, 2011) or even accretion of the nova envelope material on the secondary star (MacLeod & Ramirez-Ruiz 2015).** In this temperature asymmetry **scenario (discussed by Goranskij et al. 2002a, 2007, in application to V723 Cas), the** modulation is expected to become more prominent as the envelope dissipates and the photosphere approaches the binary. The modulation is expected to disappear or get replaced by the irradiation effect once the photosphere shrinks below the binary separation.

3. The emitting region might be larger than the binary, opaque and isothermal, but not perfectly symmetric with respect to the binary orbital revolution axis. For example, it might be slightly elongated along the direction of the line connecting the binary components. This would result in ellipsoidal variability produced by the non-spherical common envelope, rather than the distorted secondary. This scenario implies two humps per orbital period. As

the photosphere shrinks, the modulation should become more pronounced and eventually get replaced by the single hump-per-period irradiation effect once the photosphere shrinks below the binary separation.

As the nova eruption involves a prolonged phase of mass ejection (§ 1.2), there are multiple ways for an azimuthal asymmetry — the scenario 3 above — to be imprinted in the expanding nova ejecta and modulated with the binary orbital motion. Fabian & Pringle (1977) first pointed out that part of the white dwarf wind is simply shadowed by the binary companion, which should produce a rotating spiral disturbance in the wind that may manifest itself as the periodic photometric modulation. If the wind properties change in time and the photosphere is systematically advancing or receding, this would induce a drift in the photometric modulation period. **Such drift could be responsible for the difference between the period we derived from *TESS* data (§ 3.3, equation (2)) and the period derived by Schmidt (2021a) from ground-based photometry collected mostly after the end of *TESS* Sector 41, around Peak 2 (Figure 4).**

The secondary may not only partly shadow, but also gravitationally focus the white dwarf wind. The outer envelope could have an analog of a tidal hump traveling across it with the orbital period of the underlying binary. The secondary may also produce outflow of previously bound particles of the envelope from the outer (L_2) Lagrange point (Hubová & Pejcha 2019) – a configuration known to create spiral structures in the outflow concentrated in the orbital plane of the binary (e.g., Pejcha et al. 2016b; Aydi & Mohamed 2022), with the density enhancement at the base of the spiral rotating with the binary orbital motion.

For an average nova peak absolute magnitude $M = -7.5$ (Schaefer 2022a), the corresponding 10^4 K blackbody radius is $100R_\odot$, while the component separation in a $1.5M_\odot$ total mass binary in a 3 h (6 h) orbit is $1R_\odot$ ($2R_\odot$). Slowly evolving novae, such as V606 Vul, tend to have fainter than average peak absolute magnitudes (Shafter et al. 2023). We don't know the actual absolute magnitude and parameters of the nova-hosting systems in V606 Vul, however it seems safe to assume that binary orbital separation is about a few per cent of the photospheric radius. Therefore the deviation from an azimuthally symmetric photosphere may be of the same order of magnitude. The wind travel time from the white dwarf to the photosphere is comparable to the orbital period of the binary, so the asymmetry of the outflow induced by the influence of the secondary is likely to be preserved until the outflowing particles reach the photosphere.

Binary interaction (along with the alternative scenarios involving white dwarf rotation and magnetic fields discussed by Friedjung 2011) is commonly used to explain bipolar or even more complex shapes of nova ejecta that are inferred from spectral line profile modeling (e.g., Kawakita et al. 2019; Naito et al. 2022; Harvey et al. 2023), high resolution imaging (Chomiuk et al. 2014; Nyamai et al. 2021; Munari et al. 2022a) and spatially resolved spectroscopy with integral field units (e.g., Woudt et al. 2009; Takeda et al. 2022; Santamaría et al. 2022a). However, the modeling efforts are usually concerned with large spatial scales and often assume azimuthal symmetry (Livio et al. 1990; Lloyd et al. 1997). The scenario 3 suggests an increased role of asymmetries in slower novae due to the longer period of interaction between the ejecta and the binary companion. This is consistent with the findings of Slavin et al. (1995) and Santamaría et al. (2022b) that the shells of slow novae tend to be more asymmetric compared to those of fast novae.

The drag luminosity, generated from the inspiral orbit of the companion (Nordhaus & Blackman 2006), is expected to be about 1% of the nova luminosity (§ 5 of Kato & Hachisu 1994) — comparable to the observed amplitude of the periodic modulation. This could be the heating source for the scenario 2 above.

Pulsations of the nova envelope are a completely different mechanism that could generate periodic variations (Sparks et al. 1976; Bianchini et al. 1992; Schenker & Gautschy 1998; Schenker 2002; Goranskij et al. 2002b). However, the predicted pulsation periods may be too short (Wolf et al. 2018; Rosenthal et al. 2018). An argument against the pulsations as the origin of the observed periodicity in V606 Vul is the stability of the period and phase of the variations over a relatively wide range of brightness (tied to photospheric radius).

The TESS lightcurve for V606 Vul lacks data at fainter magnitudes, limiting our ability to analyze changes in amplitude and shape of the periodic variations as a function of nova brightness (photosphere radius). The apparent disappearance of the periodic signal at the very peak of the nova lightcurve (top left panel of Figure 3) is inconclusive for model discrimination. This absence could indicate a real change in variability amplitude as well as change in relative brightness of variable and non-variable emission components (like in the "direct view of the binary" scenario 1 above).

4.4. *Toy model of non-axisymmetric nova photosphere*

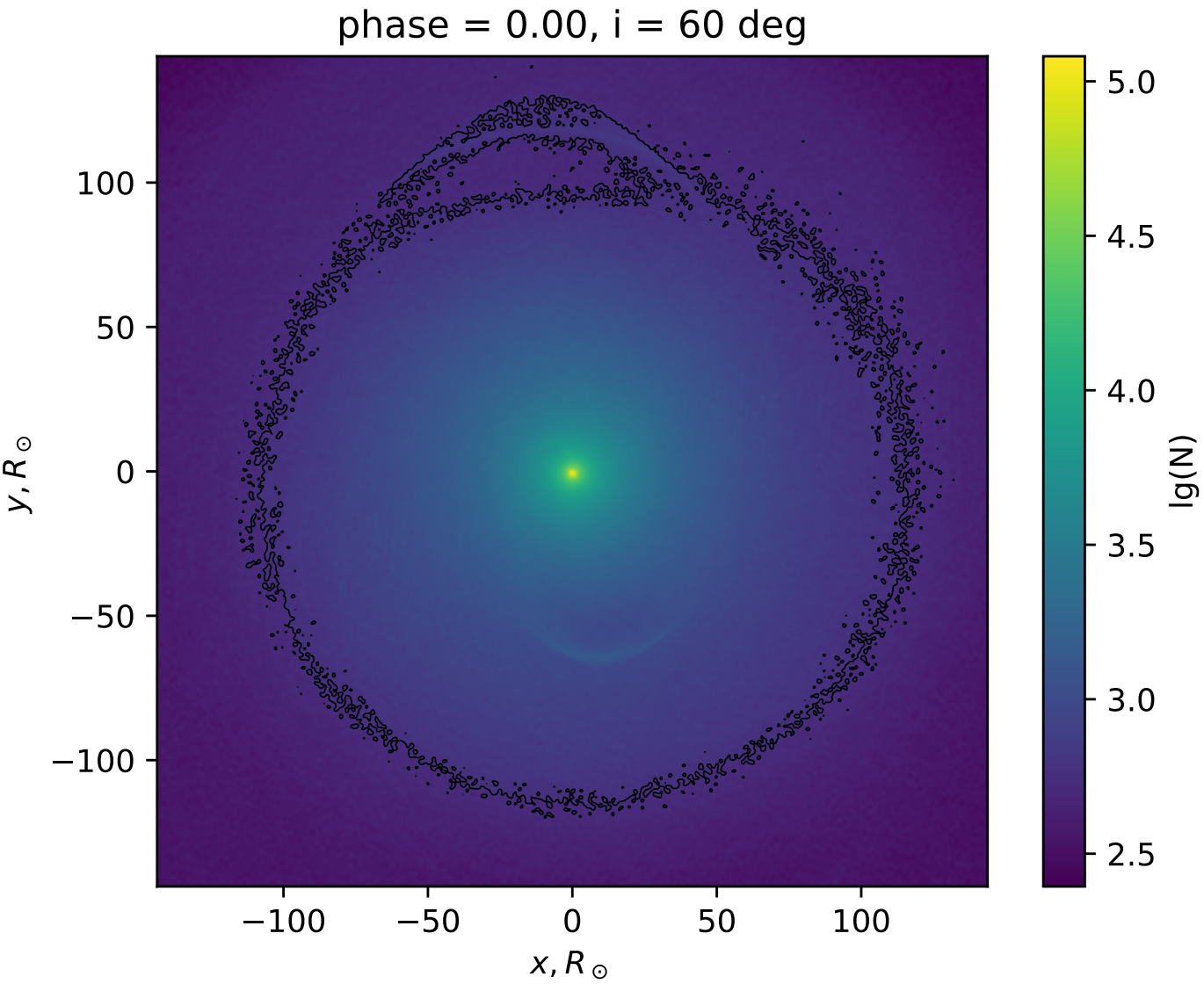

Figure 11. Simulated column density N in the image plane: the color represents number of test particles per pixel. The black curve shows a fiducial border of the photosphere at $N \simeq 560$ particles/pix.

Fabian & Pringle (1977) and Friedjung (2011) suggested that periodic modulation in a nova lightcurve can be produced by the asymmetry of the nova photosphere caused by the outflow's interaction with the secondary star. We numerically validate this scenario using a toy model of a nova wind.

We examine a case of symmetric radial outflow of matter from a white dwarf surface, parameterized by the velocity at an infinite distance, v_∞. Outflow particles do not interact with each other or with photons (no pressure or viscosity is present), but they do engage in gravitational interactions with both components of the binary system and may collide with them. This combination of gravitational interaction and shadowing induces asymmetry in the outflow. **The neglected interaction between particles is not expected to have a major impact on the overall structure of the outflow as nova winds are supersonic (e.g., Kato & Hachisu 1994; Kovetz 1998; Shaviv 2001, 2002b).**

In the stationary case that we consider, the outflow's spatial and temporal properties remain unchanged in the binary system frame, while an observer perceives the outflow's rotation with the orbital period. Due to this rotation, the nova's visible disk, a projection of the photosphere on the sky, alters its shape as well as its total area, which

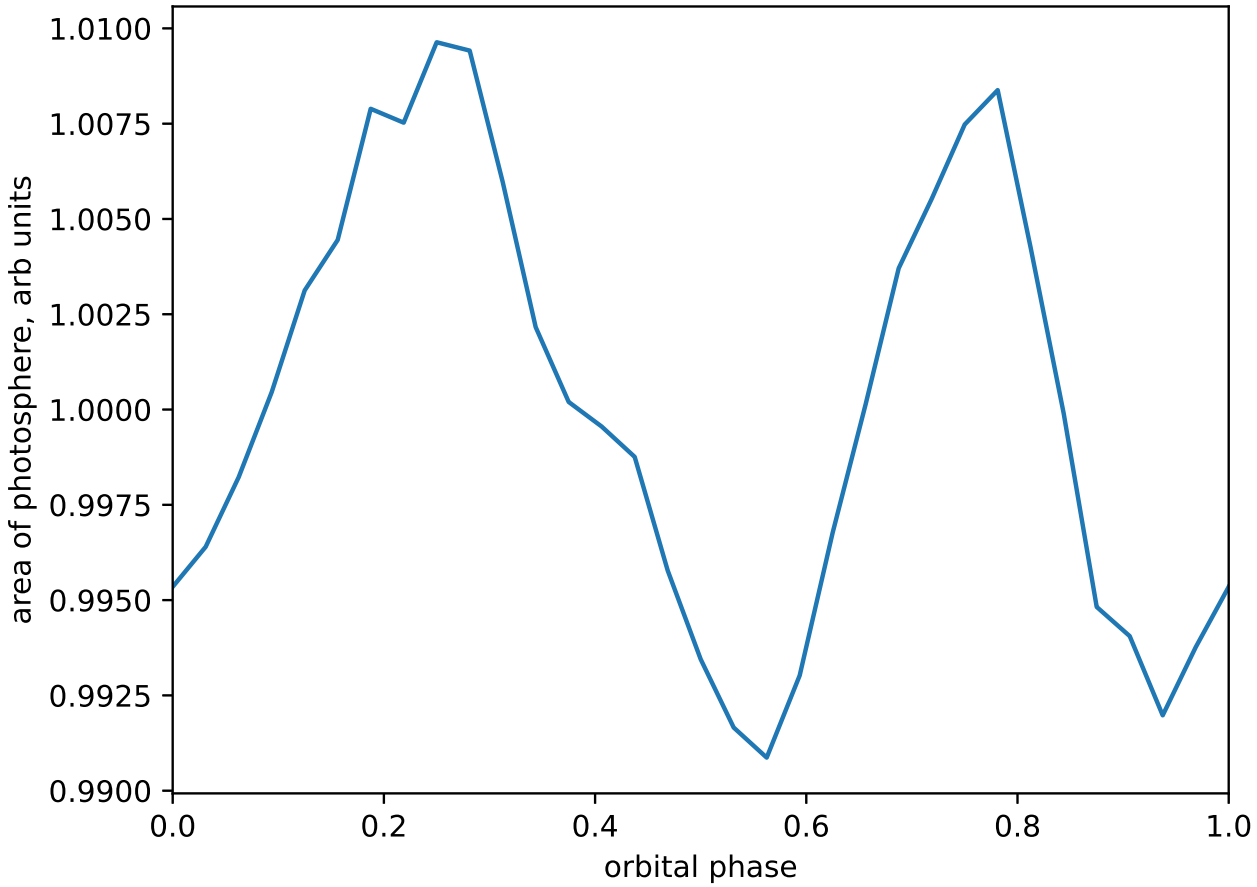

Figure 12. Simulated projected area with the column density greater than a specified value (the area enclosed by the black curve in Figure 11) as a function of binary orbital phase. The area serves as a proxy of the photosphere area that is proportional to the observed optical flux. The zero phase here corresponds to the configuration when the secondary recedes from the observer with the maximum radial velocity.

results in variability. We assume that the matter maintains a constant temperature, making the disk area a proxy for the observed flux. Normally, the limb is defined by an optical depth of 2/3, but since our model density is presented in arbitrary units, we set a fixed column density value as a threshold, so the photosphere radius is $\sim 100 R_\odot$ (corresponding to a blackbody radius of a typical nova near peak, § 4.3).

We utilize the following fiducial parameters for a nova eruption: an orbital period of 6 hours and 8 minutes (double the observed modulation period in V606 Vul), a white dwarf mass of $1 M_\odot$, a companion mass of $0.5 M_\odot$, and an outflow particle velocity at infinity $v_\infty = 1000\,\mathrm{km\,s^{-1}}$. The white dwarf radius is determined by the standard relation (Chandrasekhar 1931), while the component radius is set to correspond to Roche lobe volume (Eggleton 1983). We set inclination of the binary system to be 60°.

We ran a particle simulation with REBOUND PYTHON library (Rein & Liu 2012) with a hundred thousand test particles. The simulation was run for twenty orbital periods to let the system converge to a steady state. Since the system is stationary, we use all the particle positions during the simulation time span to populate more test particles for the consequent analysis. We set relatively small time step of a hundred seconds, which makes the total number of test particles to be 441.4 million. These particle positions were projected to a 256×256 pixel grid of the image plane with the side size of 10^{13} cm. We apply bi-cubic interpolation to scale this grid by the factor of 8 over each dimension. The count of the particles in each pixel corresponds to the column density.

Figure 11 shows such a projection for an orbital phase 0. The photosphere is the area enclosed by the black curve. This area is assumed to be a proxy to the observed optical flux from the nova. We perform this analysis for the linear grid of 32 orbital phases. Figure 12 presents the simulated photosphere area as a function of the binary orbital phase. The simulation produces a complex variability pattern with two maxima per orbital period and a full amplitude of 0.02. The JUPYTER notebook with the model and photosphere shape plots at multiple phases may be found at https://github.com/hombit/v606-vul-sims

With this toy model we do not aim to reproduce the actual phased lightcurve of V606 Vul (Figure 7), as many physical parameters of the system and its orientation are uncertain. Rather, we use the toy model to validate the idea that producing variability with an amplitude observed in V606 Vul via a rotating non-axisymmetric photosphere is perfectly possible under reasonable physical assumptions. We note that the toy model does not account for hydrodynamic pressure forces, which may smooth the photosphere shape more than the test-particle calculation suggests. Figueira et al. (2018) performed a detailed modeling of the interaction between nova ejecta and the donor star, as well as with the accretion disk. However, the authors focused on accretion disk survival and chemical contamination of the donor, without commenting on how this interaction might affect the shape of the optical photosphere.

4.5. *Flares in novae*

The novae are historically divided into "fast" and "slow" depending on time it takes them to decline by two magnitudes from the peak brightness, t_2. Fast novae ($t_2 < 80$ d) tend to display a smooth peak followed by a smooth decline before entering what is referred to as "transition phase" (see below). Slow novae ($t_2 > 80$ d) often display what appears to be a series of distinct flares on top of a nearly-constant brightness period, reaching the peak brightness during one of these flares (rather than right after the initial rise). If there are multiple flares reaching about the same magnitude they are referred as multiple peaks.

Examples of such slow novae include HR Del, V1548 Aql, V723 Cas, V5558 Sgr (Poggiani 2018), V1391 Cas (Dubovský et al. 2021), V1405 Cas (Valisa et al. 2023), V5668 Sgr (Takeda et al. 2022), V612 Sct (Mason et al. 2020), V5852 Sgr (Aydi et al. 2016). Csák et al. (2005) used the term "mini-outbursts" to describe V4745 Sgr, while Aydi et al. (2019) coined the term "mini-flares" describing nova ASASSN-17pf (LMCN 2017-11a). Figure 4 suggests that V606 Vul belongs to this list of slow "flaring" novae.

Irregular variability is often associated with the transition phase (when a nova changes from stellar-like toward a nebular spectrum) that starts 3 to 4 mag below the peak (Mclaughlin 1949). Physically, the transition phase roughly corresponds to the stage when the optical photosphere shrinks to the size of the binary, so the companion star can disturb the envelope possibly producing a complex variability pattern (see § 3.7 of Shaviv 2001). Alternatively, the complex variability may result from the induced convection in the stagnating wind when the declining luminosity of the central source becomes insufficient to accelerate wind all the way to the escape velocity (Owocki & Gayley 1997; Shaviv 2001). Retter (2002a,b); Mason et al. (2012) argued that variability during the transition phase is related to re-formation of an accretion disk disrupted by the nova. Chochol et al. (2003) suggested that flares may be triggered by enhanced accretion induced by a periastron passage of a third body.

The spectra of V606 Vul presented in Figure 5 and 6 display prominent P Cygni profiles right after the pre-maximum halt (t_0+1–8 d), then after a short break again at the rise towards Peak 1 (t_0+12–14 d). The P Cygni profiles disappear on t_0+21 d and, after yet another pause, reappear on t_0+50 d when the rise to Peak 2 begins. The appearance of new P Cygni profiles (normally found before a nova reaches its peak brightness) might suggest that Peak 1 and Peak 2 in the lightcurve of V606 Vul, as well as its initial rise, were associated with episodes of mass ejection. Previously, multiple mass-ejection episodes were reported based on spectroscopy of the multi-peak novae V4745 Sgr (Csák et al. 2005), V2362 Cyg (Lynch et al. 2008), V458 Vul (Tarasova 2015), and V659 Sct (Munari et al. 2022b), whereas other multi-peak novae V1494 Aql (Iijima & Esenoglu 2003) and V5588 Sgr (Munari et al. 2015) showed no evidence of multiple ejections in their spectra.

4.6. *The origin of mini-flares in V606 Vul*

Whereas the peaks (flares that last many days) in V606 Vul and a number of previously observed novae can be associated with mass ejection episodes, it is unclear if the same is true for the smaller and shorter flares. The flares in novae may have a wide range of timescales. In ASASSN-17pf the mini-flares last a few days, whereas the larger flares referred by Aydi et al. (2019) as maxima are a few times longer. The lightcurve of V606 Vul (Figure 4) shows flares ranging in timescale from ~ 10 days (the two maxima) to a couple of orbital periods of the binary. It is notable that

the *TESS* lightcurve of V606 Vul shows no super-short flares that would span less than an orbital period. This hints that whatever the flare is, it's an event affecting an entire photosphere rather than happening in a localized region above it (like chromospheric flares on solar-type stars; e.g., Gershberg 2005). The bottom right panel of Figure 3 displays the mini-flare on $t_0 + 31$ d and a series of mini-flares on $t_0 + 32$ d separated by three humps of the periodic variation with consequently increasing amplitude from 0.018 to 0.038 mag peak-to-through at nearly constant mean brightness. This might be a hint that the same light source is responsible for both the periodic variations and flares (like the photosphere that is expanding or heating non-uniformly) rather than two distinct sources of light (the nova shell and the directly visible binary – a possibility discussed in § 4.3).

The power spectrum (§ 3.4) and structure function (§ 3.5) of V606 Vul have a constant slope from the timescale of 8–10 d (that may correspond to the major peaks) down to the orbital period and beyond, hinting that a single physical mechanism may be producing variations at these timescales (the argument previously invoked by Schaefer 2023b). If the mini-flares of V606 Vul are scaled-down versions of its major peaks, the mini-flares might be the smaller episodes of mass ejection.

It is unclear what physical mechanism may produce multiple ejections. One possibility is that restarted unstable accretion, or fallback of the earlier-ejected but not unbound material may modulate nuclear burning rate at the white dwarf. The latter scenario was modeled by Prialnik & Livio (1995); Hillman et al. (2014) and discussed by Pejcha (2009). Sokoloski et al. (2006) and Aydi et al. (2022) discussed nuclear burning triggered by enhanced accretion outside an ongoing nova eruption.

Perhaps the closest analog to the mini-flares revealed by the *TESS* lightcurve of V606 Vul are the flares in V906 Car that lasted 1–3 days and were traced thanks to *BRITE* space-based photometry (Aydi et al. 2020b). The V906 Car flares were associated with shocks that are likely (but not necessarily) produced by new ejection episodes.

5. CONCLUSIONS

We present the first detailed analysis of a nova eruption lightcurve observed by the space photometry mission *TESS*. The slow nova V606 Vul was observed in *TESS* Sector 41, 9 to 36 days after the start of the eruption and covering the first of the two near equally-bright peaks of the nova that occurred at day 19 of the eruption (the second peak was reached on day 64).

To get confidence in our *TESS* analysis results we compare four codes implementing aperture photometry and image subtraction and cross-check the results against ground-based data (§ 3.1). The four codes produce consistent results with the remaining differences attributable to the aperture shape used and the details of background modeling (§ 3.1). Finally we use von Neumann's smoothness parameter, eqn. (1), to solve two common practical problems in photometry: selecting an optimal aperture size (§ 2.1.4) and finding magnitude zero-point offsets between observers (§ 2.2).

Thanks to the high photometric precision and weeks-long uninterrupted observations, *TESS* data reveal two distinct patterns of variability overlaid on the long-term evolution of V606 Vul (§ 3.2):

1. A series of isolated flares separated by intervals of relative quiescence (undisturbed periodic and smooth long-term variations). The smoothness of the variability power spectrum and structure function over a wide range of timescales hints that these flares may be minor mass ejection events akin to the two nova peaks that we spectroscopically associate with major mass ejection episodes (§ 4.6).

2. Stable periodic variations that present both before and after the peak and disappear only while V606 Vul is within one magnitude of its peak brightness. This photometric modulation may be caused by a slight asymmetry in the shape of the photosphere induced by the orbital motion of the underlying binary system (§ 4.4). However alternative explanations including an azimuthal asymmetry in the temperature (rather than shape) of the photosphere and unusual shape of the ejecta allowing direct view of the binary at some angles cannot be ruled out 4.4.

We conclude that an orbital period of a nova-hosting binary in some cases may be derived from precision time-series photometry when the nova is still within a few magnitudes of its peak brightness. However, the available information is insufficient to determine if the orbital period of V606 Vul is 0.12771 d (3 h 3 min 54 s, placing it near the peak of the observed orbital period distribution for novae § 4.2) or twice as long. Further space-based photometric observations are needed to determine how typical the low-amplitude periodic modulation and mini-flares are among novae.

We thank Elizabeth O. Waagen and Dr. Brian K. Kloppenborg for their assistance in communicating with the AAVSO observers, Dr. Nicole E. Schanche **and Dr. Christina L. Hedges** for the insightful discussions of *TESS* data analysis. We acknowledge with thanks the variable star observations from the AAVSO International Database contributed by observers worldwide and used in this research.

This paper includes data collected with the *TESS* mission, obtained from the MAST archive at STScI: 10.17909/0cp4-2j79. Funding for the *TESS* mission is provided by the NASA Explorer Program. STScI is operated by the Association of Universities for Research in Astronomy, Inc., under NASA contract NAS 5-26555. Based on observations 10.26131/IRSA539 obtained with the Samuel Oschin Telescope 48″ and the 60″ Telescope at the Palomar Obs. as part of the ZTF project supported by the NSF Grants No. AST-1440341 and AST-2034437 and a collaboration including current partners Caltech, IPAC, the Weizmann Inst. for Science, the Oskar Klein Center at Stockholm U., the U. of Maryland, Deutsches Elektronen-Synchrotron and Humboldt U., the TANGO Consortium of Taiwan, the U. of Wisconsin at Milwaukee, Trinity College Dublin, Lawrence Livermore National Lab., IN2P3, U. of Warwick, Ruhr U. Bochum, Northwestern U. and former partners the U. of Washington, Los Alamos National Lab., and Lawrence Berkeley National Lab. Operations are conducted by COO, IPAC, and UW. This work utilizes resources supported by the NSF's Major Research Instrumentation program, grant #1725729, as well as the U. of Illinois at Urbana-Champaign (Kindratenko et al. 2020). The work was partially performed using equipment purchased through the Moscow State U. Development Program.

This work is supported by NASA grants 80NSSC21K0775, 80NSSC22K1124, 80NSSC23K1247, and 80GSFC21M0002. E.A. acknowledges support by NASA through the NASA Hubble Fellowship grant HST-HF2-51501.001-A awarded by the Space Telescope Science Institute, which is operated by the Association of Universities for Research in Astronomy, Inc., for NASA, under contract NAS5-26555. Support was provided by Schmidt Sciences, LLC. for K.M. L.C. and B.M. are grateful for support from NSF grants AST-1751874, AST-2107070, and AST-2205628 and NASA ADAP grant 80NSSC23K0497 P.A.D acknowledges support by the grant APVV-20-0148("From Interacting Binaries to Exoplanets") of the Slovak Research and Development Agency. C.J.B. acknowledges support from NSF Award No. AST-2303803, this research award is partially funded by a generous gift of Charles Simonyi to the NSF Division of Astronomical Sciences. J.L.S. acknowledges support from NSF award AST-1816100. I.V. acknowledges support by the ETAg grants PRG2159 and PRG1006.

Facilities: TESS, AAVSO, ARAS, Asiago:Galileo, SOAR, ADS

Software: Astropy (Astropy Collaboration et al. 2013, 2018, 2022), Gnuplot. IRAF (Tody 1986), ISIS, Photutils (Bradley et al. 2016), Rebound (Rein & Liu 2012), SNAD Viewer (Malanchev et al. 2023), Source Extractor (Bertin & Arnouts 1996), TESSCut (Brasseur et al. 2019), TESSreduce (Ridden-Harper et al. 2021), VaST (Sokolovsky & Lebedev 2018), adstex, ds9 (Joye & Mandel 2003), Lightkurve (Lightkurve Collaboration et al. 2018), reproject (Robitaille et al. 2020), tequila_shots

APPENDIX

A. *TESS* TIME

A.1. *Time in* Lightkurve, tequila_shots *and* TESSreduce

Accurate timestamps associated with photometric measurements are needed for periodicity analysis and comparison of *TESS* and ground-based observations (e.g., von Essen et al. 2020), see Eastman et al. (2010) for a general discussion of timing in the context of optical photometry. The codes Lightkurve/TESSCut, tequila_shots and TESSreduce all derive the lightcurve timestamps from the keywords in the full-frame image header as

$$\mathrm{BJD(TDB)}_{\mathrm{img.\ center}} = \texttt{BJDREFI} + \texttt{BJDREFF} + (\texttt{TSTART} + \texttt{TSTOP})/2 \tag{A1}$$

The keywords `TSTART` and `TSTOP` and hence the resulting Julian Dates are expressed in Barycentric Dynamical Time (TDB) with the time and viewing direction dependent barycentric correction already applied to them. Note that the word "Barycentric" in the time system name "TDB" is referring to the time system definition[3] and is separate from the barycentric correction that is applied to the

[3] see https://naif.jpl.nasa.gov/pub/naif/toolkit_docs/FORTRAN/req/time.html

measurement timestamps. The problem with the timestamps computed with equation (A1) is that the barycentric correction that was applied to them was computed for the image center, not for the viewing direction of the target source. The difference in the barycentric correction value between the image center and the target source can be neglected for many applications: or the 8.5° distance from the center to a corner of a 12° × 12° field of view of a single *TESS* CCD chip it should not exceed 10.5 s. However, when precise timing is necessary, one needs to reverse the barycentric correction for the image center (the value of the applied correction is stored in `BARYCORR`) to get a timestamp in the reference frame of the spacecraft and then compute and apply the barycentric correction for the target source direction, as explained in § 3.3 of Handberg et al. (2021).

A.2. *Time in* VaST - *SPOC*

When processing images calibrated by the *TESS* Science Processing Operations Center (SPOC Jenkins et al. 2016) pipeline (the ones used in this work), the current version of the VaST code derives the timestamps as

$$\mathrm{BJD(UTC)}_{\mathrm{img.\ center}} = \mathrm{JD}(\texttt{DATE-OBS}) + \texttt{EXPOSURE}/(2 \times \texttt{DEADC}) \tag{A2}$$

that are expressed in UTC. Here JD(`DATE-OBS`) represents conversion from the string expressing the calendar date and time to Julian Date, `EXPOSURE` is the keyword expressing the effective on-source time and `DEADC` is the ratio of the effective to the total on-source time, that differ due to cosmic ray rejection (§ 2.1.1).

To compare the timestamps computed with equation (A2) to the ones derived form equation (A1), we add the current (for 2021) difference of 69.184 s between the Terrestrial Time (TT) and UTC to the VaST-derived UTC timestamps and neglect the periodic difference between the TT and TDB that is always less than 2 milliseconds – orders of magnitude smaller than the exposure time. The comparison confirms that the calendar date and time string in `DATE-OBS` encodes the same barycentric-corrected timestamp as `TSTART` adjusted for the shift between the UTC and TDB (or TT) time system.

A.3. *Time in* VaST - *TICA*

The alternative "*TESS* Image CAlibrator Full Frame Images" (TICA; Fausnaugh et al. 2020) have a different set of keywords describing the observing time in TDB as measured at the spacecraft: `TJD_ZERO`, `STARTTJD`, `MIDTJD`, `ENDTJD` that are supported by VaST. For TICA *TESS* images, VaST assigns the timestamps as

$$\mathrm{JD(TDB)} = \texttt{TJD\_ZERO} + \texttt{MIDTJD} \tag{A3}$$

where the Julian Dates are expressed in TDB as measured at the spacecraft, so the barycentric correction still needs to be applied to the resulting timestamps.

B. *TESS* LIGHTCURVE FIDELITY

As the accuracy of space-based photometry is typically limited by various systematic effects (§ 2.1.2), how confident can we be that the lightcurve features shown in Figures 2 and 3 - including the overall shape, mini-flares, and periodic modulation - are real? What if the four codes compared in § 3.1 faithfully extract a signal that is not intrinsic to the nova? Below, we summarize the arguments supporting the lightcurves authenticity.

- The overall shape of the *TESS* lightcurve closely follows the *I*-band lightcurve obtained by ground-based observers (Figure 4; § 3.2).
- Neither the nearby check stars nor the background lightcurve display the 0.12771 d periodic modulation (§ 3.3) or mini-flares (§ 4.6) similar to those observed in V606 Vul, see Figure 13 and the related online materials[1].
- **The periodic signal is present only in the pixels associated with the nova image (Figure 14).**
- The periodic signal and mini-flares are absent from lightcurves extracted at the V606 Vul location during sectors other than Sector 41[1], supporting their association with the nova eruption rather than contamination from nearby variable sources not expected to display unusual activity specifically during Sector 41.

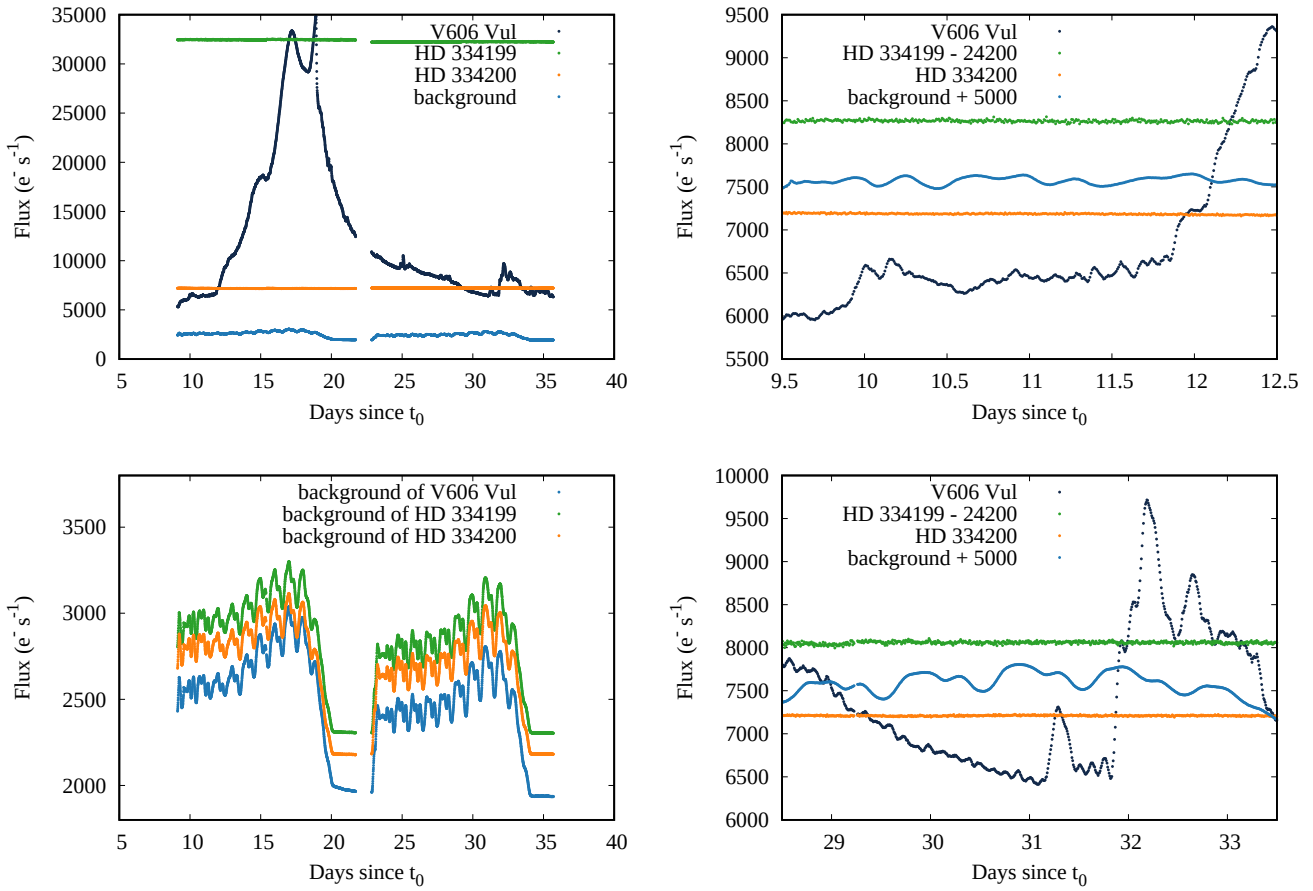

Figure 13. The top left panel displays the background-subtracted *TESS* lightcurves of V606 Vul and two nearby check stars: HD 334199 and HD 334200, as well as the background level associated with V606 Vul. The two panels on the right zoom into specific lightcurve regions before (top) and after the nova peak (bottom). The lightcurves of HD 334199 and V606 Vul background are shifted to fit in the plotting range. Once can see that the lightcurves of the two check stars show no variations comparable in amplitude and timescale to the periodic modulation and mini-flares visible in the lightcurve of V606 Vul. The bottom left panel presents the background lightcurves of V606 Vul (same as the other panels) and the two check stars. The three background lightcurves all display a similar modulation pattern with a period of about a day that is successfully subtracted as it is not visible in the background-subtracted lightcurves of the three stars. The LIGHTKURVE code used to extract these lightcurves is available online [1].

REFERENCES

Abdo, A. A., Ackermann, M., Ajello, M., et al. 2010, Science, 329, 817, doi: 10.1126/science.1192537

Acciari, V. A., Ansoldi, S., Antonelli, L. A., et al. 2022, Nature Astronomy, 6, 689, doi: 10.1038/s41550-022-01640-z

Ackermann, M., Ajello, M., Albert, A., et al. 2014, Science, 345, 554, doi: 10.1126/science.1253947

Aigrain, S., Pont, F., Fressin, F., et al. 2009, A&A, 506, 425, doi: 10.1051/0004-6361/200911885

Alard, C. 2000, A&AS, 144, 363, doi: 10.1051/aas:2000214

Alard, C., & Lupton, R. H. 1998, ApJ, 503, 325, doi: 10.1086/305984

Anderson, J., & King, I. R. 2000, PASP, 112, 1360, doi: 10.1086/316632

Antipin, S. V., Becker, I., Belinski, A. A., et al. 2018, Research in Astronomy and Astrophysics, 18, 092, doi: 10.1088/1674-4527/18/8/92

Astropy Collaboration, Robitaille, T. P., Tollerud, E. J., et al. 2013, A&A, 558, A33, doi: 10.1051/0004-6361/201322068

Astropy Collaboration, Price-Whelan, A. M., Sipőcz, B. M., et al. 2018, AJ, 156, 123, doi: 10.3847/1538-3881/aabc4f

Astropy Collaboration, Price-Whelan, A. M., Lim, P. L., et al. 2022, ApJ, 935, 167, doi: 10.3847/1538-4357/ac7c74

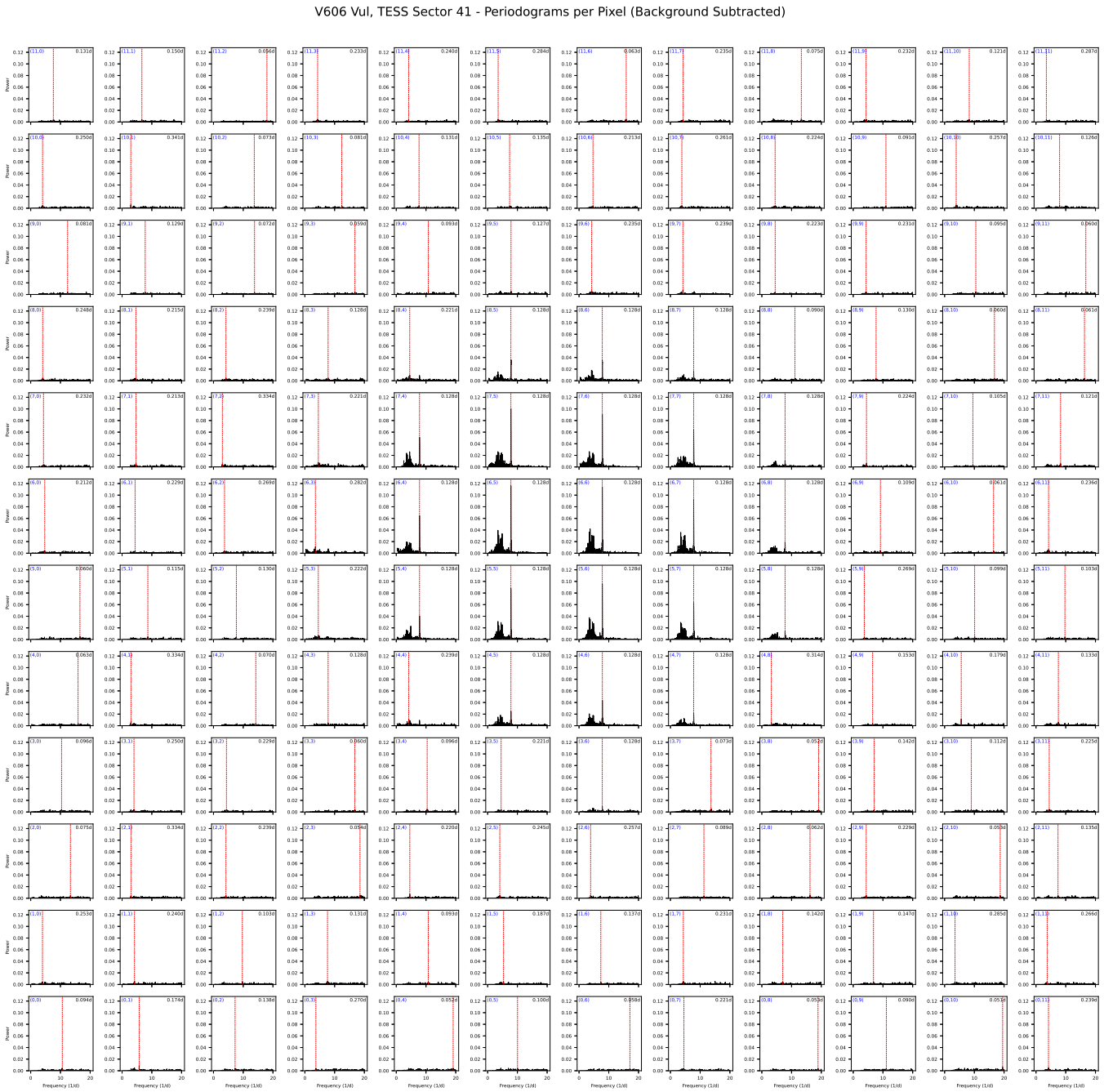

Figure 14. The grid of Lomb-Scargle periodograms constructed for background-subtracted detrended individual-pixel lightcurves. The grid of pixels corresponds to the Sector 41 image presented in Figure 1 (left panel). The blue numbers in the upper left corner of the plot denote the pixel coordinates in the cutout with (0, 0) corresponding to the lower left pixel in Figure 1 (left panel). The red dashed line in each plot indicates the highest peak in the periodogram of that pixel's lightcurve. The period corresponding to the highest peak is indicated in the top right corner of each plot. The background lightcurve extraction is described in § 2.1.3. Each pixel's lightcurve is detrended with the Savitzky-Golay filter before computing a periodogram. Flaring episodes are not excluded from the lightcurves, which produced more residual power between 2.5 and 5 cycles per day compared to Figure 7 (right panel), the power at even lower frequencies is effectively suppressed by detrending. A peak corresponding to the 0.128 d period is clearly visible in periodograms corresponding to the central pixels associated with the nova image (cf. Figure 1). The Lightkurve code used to extract these periodograms is available online[1].

Atwood, W. B., Abdo, A. A., Ackermann, M., et al. 2009, ApJ, 697, 1071, doi: 10.1088/0004-637X/697/2/1071

Aydi, E., & Mohamed, S. 2022, MNRAS, 513, 4405, doi: 10.1093/mnras/stac749

Aydi, E., Mróz, P., Whitelock, P. A., et al. 2016, MNRAS, 461, 1529, doi: 10.1093/mnras/stw1396

Aydi, E., Orio, M., Beardmore, A. P., et al. 2018, MNRAS, 480, 572, doi: 10.1093/mnras/sty1759

Aydi, E., Chomiuk, L., Strader, J., et al. 2019, arXiv e-prints, arXiv:1903.09232, doi: 10.48550/arXiv.1903.09232

Aydi, E., Chomiuk, L., Izzo, L., et al. 2020a, ApJ, 905, 62, doi: 10.3847/1538-4357/abc3bb

Aydi, E., Sokolovsky, K. V., Chomiuk, L., et al. 2020b, Nature Astronomy, 4, 776, doi: 10.1038/s41550-020-1070-y

Aydi, E., Sokolovsky, K. V., Bright, J. S., et al. 2022, ApJ, 939, 6, doi: 10.3847/1538-4357/ac913b

Aydi, E., Chomiuk, L., Strader, J., et al. 2024, MNRAS, 527, 9303, doi: 10.1093/mnras/stad3342

Baptista, R., Borges, B. W., & Oliveira, A. S. 2016, MNRAS, 463, 3799, doi: 10.1093/mnras/stw2258

Baptista, R., & Bortoletto, A. 2008, ApJ, 676, 1240, doi: 10.1086/528706

Becker, A. 2015, HOTPANTS: High Order Transform of PSF ANd Template Subtraction, Astrophysics Source Code Library, record ascl:1504.004. http://ascl.net/1504.004

Becker, A. C., Homrighausen, D., Connolly, A. J., et al. 2012, MNRAS, 425, 1341, doi: 10.1111/j.1365-2966.2012.21542.x

Bertin, E., & Arnouts, S. 1996, A&AS, 117, 393, doi: 10.1051/aas:1996164

Bhatta, G., & Dhital, N. 2020, ApJ, 891, 120, doi: 10.3847/1538-4357/ab7455

Bianchini, A., Friedjung, M., & Brinkmann, W. 1992, A&A, 257, 599

Bode, M. F., & Evans, A. 2008a, Classical Novae, Vol. 43, doi: 10.1017/CBO9780511536168

—. 2008b, Classical Novae, Vol. 43, doi: 10.1017/CBO9780511536168

Boyd, D. 2012, JAAVSO, 40, 990

Bradley, L., Sipocz, B., Robitaille, T., et al. 2016, Photutils: Photometry tools, Astrophysics Source Code Library, record ascl:1609.011. http://ascl.net/1609.011

Bramich, D. M. 2008, MNRAS, 386, L77, doi: 10.1111/j.1745-3933.2008.00464.x

Bramich, D. M., Horne, K., Alsubai, K. A., et al. 2016, MNRAS, 457, 542, doi: 10.1093/mnras/stv2910

Bramich, D. M., Horne, K., Albrow, M. D., et al. 2013, MNRAS, 428, 2275, doi: 10.1093/mnras/sts184

Brasseur, C. E., Phillip, C., Fleming, S. W., Mullally, S. E., & White, R. L. 2019, Astrocut: Tools for creating cutouts of TESS images. http://ascl.net/1905.007

Bruch, A. 1992, A&A, 266, 237

—. 2022, MNRAS, 509, 4669, doi: 10.1093/mnras/stab2675

—. 2023a, MNRAS, 519, 352, doi: 10.1093/mnras/stac3493

—. 2023b, MNRAS, 525, 1953, doi: 10.1093/mnras/stad2089

Budding, E., & Demircan, O. 2007, Introduction to Astronomical Photometry, Vol. 6

Burderi, L., Robba, N. R., Guainazzi, M., & Cusumano, G. 1993, Nuovo Cimento C Geophysics Space Physics C, 16, 675, doi: 10.1007/BF02512051

Burke, C. J., Shen, Y., Chen, Y.-C., et al. 2020, ApJ, 899, 136, doi: 10.3847/1538-4357/aba3ce

Burke, C. J., Shen, Y., Blaes, O., et al. 2021, Science, 373, 789, doi: 10.1126/science.abg9933

Calamida, A., Matheson, T., Olszewski, E. W., et al. 2022, ApJ, 940, 19, doi: 10.3847/1538-4357/ac96f4

Caplar, N., Lilly, S. J., & Trakhtenbrot, B. 2017, ApJ, 834, 111, doi: 10.3847/1538-4357/834/2/111

Chandrasekhar, S. 1931, ApJ, 74, 81, doi: 10.1086/143324

Chen, H.-L., Woods, T. E., Yungelson, L. R., Gilfanov, M., & Han, Z. 2016, MNRAS, 458, 2916, doi: 10.1093/mnras/stw458

Chochol, D., Pribulla, T., Parimucha, Š., & Vaňko, M. 2003, Baltic Astronomy, 12, 610, doi: 10.1515/astro-2017-0089

Chomiuk, L., Metzger, B. D., & Shen, K. J. 2021a, ARA&A, 59, 391, doi: 10.1146/annurev-astro-112420-114502

Chomiuk, L., Linford, J. D., Yang, J., et al. 2014, Nature, 514, 339, doi: 10.1038/nature13773

Chomiuk, L., Linford, J. D., Aydi, E., et al. 2021b, ApJS, 257, 49, doi: 10.3847/1538-4365/ac24ab

Clemens, J. C., Crain, J. A., & Anderson, R. 2004, in Proc. SPIE, Vol. 5492, Ground-based Instrumentation for Astronomy, ed. A. F. M. Moorwood & M. Iye, 331–340, doi: 10.1117/12.550069

Collier, S., & Peterson, B. M. 2001, ApJ, 555, 775, doi: 10.1086/321517

Contini, M., & Prialnik, D. 1997, ApJ, 475, 803, doi: 10.1086/303555

Csák, B., Kiss, L. L., Retter, A., Jacob, A., & Kaspi, S. 2005, A&A, 429, 599, doi: 10.1051/0004-6361:20035751

Darnley, M. J., Henze, M., Bode, M. F., et al. 2016, ApJ, 833, 149, doi: 10.3847/1538-4357/833/2/149

De, K., Kasliwal, M. M., Hankins, M. J., et al. 2021, ApJ, 912, 19, doi: 10.3847/1538-4357/abeb75

De, K., Soria, R., Agusti, M. B., et al. 2022, The Astronomer's Telegram, 15587, 1
De Young, J. A., & Schmidt, R. E. 1994, ApJL, 431, L47, doi: 10.1086/187469
Deeming, T. J. 1975, Ap&SS, 36, 137, doi: 10.1007/BF00681947
Della Valle, M., & Izzo, L. 2020, A&A Rv, 28, 3, doi: 10.1007/s00159-020-0124-6
Deming, D., Knutson, H., Kammer, J., et al. 2015, ApJ, 805, 132, doi: 10.1088/0004-637X/805/2/132
Derdzinski, A. M., Metzger, B. D., & Lazzati, D. 2017, MNRAS, 469, 1314, doi: 10.1093/mnras/stx829
Dobrotka, A., Mineshige, S., & Casares, J. 2012, MNRAS, 420, 2467, doi: 10.1111/j.1365-2966.2011.20210.x
Dodin, A. V., Potanin, S. A., Shatsky, N. I., et al. 2020, Astronomy Letters, 46, 429, doi: 10.1134/S106377372007004X
Dubovský, P. A., Medulka, T., & Kudzej, I. 2021, Open European Journal on Variable Stars, 220, 37, doi: 10.5817/OEJV2021-0220
Eastman, J., Siverd, R., & Gaudi, B. S. 2010, PASP, 122, 935, doi: 10.1086/655938
Eggleton, P. P. 1983, ApJ, 268, 368, doi: 10.1086/160960
Elsworth, Y., & James, J. F. 1986, MNRAS, 220, 895, doi: 10.1093/mnras/220.4.895
Emmanoulopoulos, D., McHardy, I. M., & Uttley, P. 2010, MNRAS, 404, 931, doi: 10.1111/j.1365-2966.2010.16328.x
Eyres, S. P. S., Bewsher, D., Hillman, Y., et al. 2017, MNRAS, 467, 2684, doi: 10.1093/mnras/stx298
Fabian, A. C., & Pringle, J. E. 1977, MNRAS, 180, 749, doi: 10.1093/mnras/180.4.749
Fausnaugh, M. M., Burke, C. J., Ricker, G. R., & Vanderspek, R. 2020, Research Notes of the American Astronomical Society, 4, 251, doi: 10.3847/2515-5172/abd63a
Figueira, J., José, J., García-Berro, E., et al. 2018, A&A, 613, A8, doi: 10.1051/0004-6361/201731545
Franckowiak, A., Jean, P., Wood, M., Cheung, C. C., & Buson, S. 2018, A&A, 609, A120, doi: 10.1051/0004-6361/201731516
Friedjung, M. 1987, A&A, 180, 155
—. 1990, in IAU Colloq. 122: Physics of Classical Novae, ed. A. Cassatella & R. Viotti, Vol. 369, 244, doi: 10.1007/3-540-53500-4_132
—. 2004, Baltic Astronomy, 13, 116
—. 2011, A&A, 536, A97, doi: 10.1051/0004-6361/201016397
Fuentes-Morales, I., Tappert, C., Zorotovic, M., et al. 2021, MNRAS, 501, 6083, doi: 10.1093/mnras/staa3482
Gaia Collaboration, Prusti, T., de Bruijne, J. H. J., et al. 2016, A&A, 595, A1, doi: 10.1051/0004-6361/201629272
Gaia Collaboration, Vallenari, A., Brown, A. G. A., et al. 2023, A&A, 674, A1, doi: 10.1051/0004-6361/202243940
Gal-Yam, A., Maoz, D., Guhathakurta, P., & Filippenko, A. V. 2008, ApJ, 680, 550, doi: 10.1086/587680
Gallagher, J. S., I., & Code, A. D. 1974, ApJ, 189, 303, doi: 10.1086/152804
Gangestad, J. W., Henning, G. A., Persinger, R. R., & Ricker, G. R. 2013, arXiv e-prints, arXiv:1306.5333. https://arxiv.org/abs/1306.5333
Gershberg, R. E. 2005, Solar-Type Activity in Main-Sequence Stars, doi: 10.1007/3-540-28243-2
Giroletti, M., Munari, U., Körding, E., et al. 2020, A&A, 638, A130, doi: 10.1051/0004-6361/202038142
González-Martín, O., & Vaughan, S. 2012, A&A, 544, A80, doi: 10.1051/0004-6361/201219008
Gopalan, G., Plavchan, P., van Eyken, J., et al. 2016, PASP, 128, 084504, doi: 10.1088/1538-3873/128/966/084504
Goranskij, V. P., Katysheva, N. A., Kusakin, A. V., et al. 2002a, in Astronomical Society of the Pacific Conference Series, Vol. 261, The Physics of Cataclysmic Variables and Related Objects, ed. B. T. Gänsicke, K. Beuermann, & K. Reinsch, 625
Goranskij, V. P., Metlova, N. V., & Shugarov, S. Y. 2002b, in American Institute of Physics Conference Series, Vol. 637, Classical Nova Explosions, ed. M. Hernanz & J. José, 311–314, doi: 10.1063/1.1518221
Goranskij, V. P., Shugarov, S. Y., Katysheva, N. A., et al. 2000, Information Bulletin on Variable Stars, 4852, 1
Goranskij, V. P., Katysheva, N. A., Kusakin, A. V., et al. 2007, Astrophysical Bulletin, 62, 125, doi: 10.1134/S1990341307020046
Gorbatskii, V. G. 1972, Soviet Ast., 16, 32
Gordon, A. C., Aydi, E., Page, K. L., et al. 2021, ApJ, 910, 134, doi: 10.3847/1538-4357/abe547
Goyal, A., Soida, M., Stawarz, Ł., et al. 2022, ApJ, 927, 214, doi: 10.3847/1538-4357/ac4d95
Graham, M. J., Djorgovski, S. G., Drake, A. J., et al. 2014, MNRAS, 439, 703, doi: 10.1093/mnras/stt2499
Guevel, D., & Hosseinzadeh, G. 2017, Dguevel/Pyzogy: Initial Release, v0.0.1, Zenodo, Zenodo, doi: 10.5281/zenodo.1043973
Gupta, A. C., Krichbaum, T. P., Wiita, P. J., et al. 2012, MNRAS, 425, 1357, doi: 10.1111/j.1365-2966.2012.21550.x
H. E. S. S. Collaboration, Aharonian, F., Ait Benkhali, F., et al. 2022, Science, 376, 77, doi: 10.1126/science.abn0567

Hachisu, I., & Kato, M. 2022, ApJ, 939, 1, doi: 10.3847/1538-4357/ac9475
Handberg, R., Lund, M. N., White, T. R., et al. 2021, AJ, 162, 170, doi: 10.3847/1538-3881/ac09f1
Harrison, T. E., & Campbell, R. K. 2016, MNRAS, 459, 4161, doi: 10.1093/mnras/stw961
Harvey, É. J., Aydi, E., Izzo, L., et al. 2023, MNRAS, 521, 4750, doi: 10.1093/mnras/stad825
Hattori, S., Foreman-Mackey, D., Hogg, D. W., et al. 2022, AJ, 163, 284, doi: 10.3847/1538-3881/ac625a
Henden, A., & Munari, U. 2014, Contributions of the Astronomical Observatory Skalnate Pleso, 43, 518
Hillman, Y., Prialnik, D., Kovetz, A., Shara, M. M., & Neill, J. D. 2014, MNRAS, 437, 1962, doi: 10.1093/mnras/stt2027
Hillman, Y., Shara, M. M., Prialnik, D., & Kovetz, A. 2020, Nature Astronomy, 4, 886, doi: 10.1038/s41550-020-1062-y
Hippke, M., David, T. J., Mulders, G. D., & Heller, R. 2019, AJ, 158, 143, doi: 10.3847/1538-3881/ab3984
Hitchcock, J. A., Hundertmark, M., Foreman-Mackey, D., et al. 2021, MNRAS, 504, 3561, doi: 10.1093/mnras/stab1114
Holdsworth, D. L., Rushton, M. T., Bewsher, D., et al. 2014, MNRAS, 438, 3483, doi: 10.1093/mnras/stt2455
Hounsell, R., Bode, M. F., Hick, P. P., et al. 2010, ApJ, 724, 480, doi: 10.1088/0004-637X/724/1/480
Hounsell, R., Darnley, M. J., Bode, M. F., et al. 2016, ApJ, 820, 104, doi: 10.3847/0004-637X/820/2/104
Hu, L., Wang, L., Chen, X., & Yang, J. 2022, ApJ, 936, 157, doi: 10.3847/1538-4357/ac7394
Hubová, D., & Pejcha, O. 2019, MNRAS, 489, 891, doi: 10.1093/mnras/stz2208
Hughes, P. A., Aller, H. D., & Aller, M. F. 1992, ApJ, 396, 469, doi: 10.1086/171734
Iijima, T., & Esenoglu, H. H. 2003, A&A, 404, 997, doi: 10.1051/0004-6361:20030528
Itagaki, K., Schmeer, P., Watanabe, F., et al. 2021, Central Bureau Electronic Telegrams, 5007
Jenkins, J. M., Twicken, J. D., McCauliff, S., et al. 2016, in Society of Photo-Optical Instrumentation Engineers (SPIE) Conference Series, Vol. 9913, Software and Cyberinfrastructure for Astronomy IV, ed. G. Chiozzi & J. C. Guzman, 99133E, doi: 10.1117/12.2233418
Joye, W. A., & Mandel, E. 2003, in Astronomical Society of the Pacific Conference Series, Vol. 295, Astronomical Data Analysis Software and Systems XII, ed. H. E. Payne, R. I. Jedrzejewski, & R. N. Hook, 489
Kato, M., & Hachisu, I. 1994, ApJ, 437, 802, doi: 10.1086/175041
—. 2011, ApJ, 743, 157, doi: 10.1088/0004-637X/743/2/157
Kato, T. 2023, arXiv e-prints, arXiv:2305.01197, doi: 10.48550/arXiv.2305.01197
Kawakita, H., Shinnaka, Y., Arai, A., Arasaki, T., & Ikeda, Y. 2019, ApJ, 872, 120, doi: 10.3847/1538-4357/aaff68
Kawash, A., Chomiuk, L., Strader, J., et al. 2021, ApJ, 910, 120, doi: 10.3847/1538-4357/abe53d
—. 2022, ApJ, 937, 64, doi: 10.3847/1538-4357/ac8d5e
Kim, D.-W., Protopapas, P., Alcock, C., Byun, Y.-I., & Bianco, F. B. 2009, MNRAS, 397, 558, doi: 10.1111/j.1365-2966.2009.14967.x
Kindratenko, V., Mu, D., Zhan, Y., et al. 2020, in Practice and experience in advanced research computing, 41–48
Kloppenborg, B. K. 2022, Observations from the AAVSO International Database, https://www.aavso.org
Kochanek, C. S., Shappee, B. J., Stanek, K. Z., et al. 2017, PASP, 129, 104502, doi: 10.1088/1538-3873/aa80d9
Kolesnikova, D. M., Sat, L. A., Sokolovsky, K. V., Antipin, S. V., & Samus, N. N. 2008, AcA, 58, 279, doi: 10.48550/arXiv.0809.4153
Kovács, G., Bakos, G., & Noyes, R. W. 2005, MNRAS, 356, 557, doi: 10.1111/j.1365-2966.2004.08479.x
Kovetz, A. 1998, ApJ, 495, 401, doi: 10.1086/305280
Kozłowski, S. 2016, ApJ, 826, 118, doi: 10.3847/0004-637X/826/2/118
Krishnamurthy, A., Villasenor, J., Seager, S., Ricker, G., & Vanderspek, R. 2019, Acta Astronautica, 160, 46, doi: 10.1016/j.actaastro.2019.04.016
Krishnan, S., Markowitz, A. G., Schwarzenberg-Czerny, A., & Middleton, M. J. 2021, MNRAS, 508, 3975, doi: 10.1093/mnras/stab2839
Lafler, J., & Kinman, T. D. 1965, ApJS, 11, 216, doi: 10.1086/190116
Lance, C. M., McCall, M. L., & Uomoto, A. K. 1988, ApJS, 66, 151, doi: 10.1086/191251
Landolt, A. U. 1992, AJ, 104, 340, doi: 10.1086/116242
Law, N. M., Fors, O., Wulfken, P., Ratzloff, J., & Kavanaugh, D. 2014, in Society of Photo-Optical Instrumentation Engineers (SPIE) Conference Series, Vol. 9145, Ground-based and Airborne Telescopes V, ed. L. M. Stepp, R. Gilmozzi, & H. J. Hall, 91450Z, doi: 10.1117/12.2057031
Li, K.-L., Metzger, B. D., Chomiuk, L., et al. 2017, Nature Astronomy, 1, 697, doi: 10.1038/s41550-017-0222-1
Lightkurve Collaboration, Cardoso, J. V. d. M., Hedges, C., et al. 2018, Lightkurve: Kepler and TESS time series analysis in Python, Astrophysics Source Code Library. http://ascl.net/1812.013
Lindegren, L., & Lindgren, H. 1975, Nature, 258, 501, doi: 10.1038/258501a0

Livio, M. 1990, in IAU Colloq. 122: Physics of Classical Novae, ed. A. Cassatella & R. Viotti, Vol. 369, 342, doi: 10.1007/3-540-53500-4_146
Livio, M., Shankar, A., Burkert, A., & Truran, J. W. 1990, ApJ, 356, 250, doi: 10.1086/168836
Lloyd, H. M., O'Brien, T. J., & Bode, M. F. 1997, MNRAS, 284, 137, doi: 10.1093/mnras/284.1.137
Lomb, N. R. 1976, Ap&SS, 39, 447, doi: 10.1007/BF00648343
Luger, R., Kruse, E., Foreman-Mackey, D., Agol, E., & Saunders, N. 2018, AJ, 156, 99, doi: 10.3847/1538-3881/aad230
Luna, G. J. M., Lima, I. J., & Orio, M. 2024, Boletin de la Asociacion Argentina de Astronomia La Plata Argentina, 65, 60, doi: 10.48550/arXiv.2310.02220
Lynch, D. K., Woodward, C. E., Gehrz, R., et al. 2008, AJ, 136, 1815, doi: 10.1088/0004-6256/136/5/1815
Lyubarskii, Y. E. 1997, MNRAS, 292, 679, doi: 10.1093/mnras/292.3.679
MacDonald, J. 1980, MNRAS, 191, 933, doi: 10.1093/mnras/191.4.933
MacLeod, C. L., Ivezić, Ž., Kochanek, C. S., et al. 2010, ApJ, 721, 1014, doi: 10.1088/0004-637X/721/2/1014
MacLeod, M., & Ramirez-Ruiz, E. 2015, ApJ, 803, 41, doi: 10.1088/0004-637X/803/1/41
Malanchev, K., Kornilov, M. V., Pruzhinskaya, M. V., et al. 2023, PASP, 135, 024503, doi: 10.1088/1538-3873/acb292
Martin, P., Dubus, G., Jean, P., Tatischeff, V., & Dosne, C. 2018, A&A, 612, A38, doi: 10.1051/0004-6361/20173169210.48550/arXiv.1710.05515
Masci, F. J., Laher, R. R., Rusholme, B., et al. 2019, PASP, 131, 018003, doi: 10.1088/1538-3873/aae8ac
Mason, E., Ederoclite, A., Williams, R. E., Della Valle, M., & Setiawan, J. 2012, A&A, 544, A149, doi: 10.1051/0004-6361/201219556
Mason, E., Shore, S. N., De Gennaro Aquino, I., et al. 2018, ApJ, 853, 27, doi: 10.3847/1538-4357/aaa247
Mason, E., Shore, S. N., Kuin, P., & Bohlsen, T. 2020, A&A, 635, A115, doi: 10.1051/0004-6361/201937025
Max-Moerbeck, W., Richards, J. L., Hovatta, T., et al. 2014a, MNRAS, 445, 437, doi: 10.1093/mnras/stu1707
Max-Moerbeck, W., Hovatta, T., Richards, J. L., et al. 2014b, MNRAS, 445, 428, doi: 10.1093/mnras/stu1749
Mazeh, T., Tamuz, O., & Zucker, S. 2007, in Astronomical Society of the Pacific Conference Series, Vol. 366, Transiting Extrapolar Planets Workshop, ed. C. Afonso, D. Weldrake, & T. Henning, 119. https://arxiv.org/abs/astro-ph/0612418
Mclaughlin, D. B. 1947, PASP, 59, 244, doi: 10.1086/125957
—. 1949, PASP, 61, 74, doi: 10.1086/126128
McLaughlin, D. B. 1956, Vistas in Astronomy, 2, 1477, doi: 10.1016/0083-6656(56)90076-9
Mennickent, R. E., & Honeycutt, R. K. 1995, Information Bulletin on Variable Stars, 4232, 1
Metzger, B. D., Caprioli, D., Vurm, I., et al. 2016, MNRAS, 457, 1786, doi: 10.1093/mnras/stw123
Metzger, B. D., Hascoët, R., Vurm, I., et al. 2014, MNRAS, 442, 713, doi: 10.1093/mnras/stu844
Mönkkönen, J., Tsygankov, S. S., Mushtukov, A. A., et al. 2022, MNRAS, 515, 571, doi: 10.1093/mnras/stac1828
Mukai, K., & Sokoloski, J. L. 2019, Physics Today, 72, 38, doi: 10.1063/PT.3.4341
Munari, U., Dallaporta, S., & Castellani, F. 2010, Information Bulletin on Variable Stars, 5930, 1, doi: 10.48550/arXiv.1003.2870
Munari, U., Dallaporta, S., Castellani, F., et al. 2013, MNRAS, 435, 771, doi: 10.1093/mnras/stt1340
Munari, U., Giroletti, M., Marcote, B., et al. 2022a, A&A, 666, L6, doi: 10.1051/0004-6361/202244821
Munari, U., Henden, A., Banerjee, D. P. K., et al. 2015, MNRAS, 447, 1661, doi: 10.1093/mnras/stu2486
Munari, U., & Moretti, S. 2012, Baltic Astronomy, 21, 22, doi: 10.1515/astro-2017-0354
Munari, U., Moretti, S., & Maitan, A. 2020, A&A, 639, L10, doi: 10.1051/0004-6361/202038403
Munari, U., Moretti, S., Maitan, A., & Andreoli, V. 2021a, The Astronomer's Telegram, 14816, 1
Munari, U., Righetti, G. L., & Dallaporta, S. 2022b, MNRAS, 516, 4805, doi: 10.1093/mnras/stac2469
Munari, U., Vagnozzi, A., & Valisa, P. 2021b, The Astronomer's Telegram, 14793, 1
Munari, U., Bacci, S., Baldinelli, L., et al. 2012, Baltic Astronomy, 21, 13, doi: 10.1515/astro-2017-0353
Murphy-Glaysher, F. J., Darnley, M. J., Harvey, É. J., et al. 2022, MNRAS, 514, 6183, doi: 10.1093/mnras/stac1577
Naito, H., Tajitsu, A., Ribeiro, V. A. R. M., et al. 2022, ApJ, 932, 39, doi: 10.3847/1538-4357/ac6c82
Nelson, L. A., MacCannell, K. A., & Dubeau, E. 2004, ApJ, 602, 938, doi: 10.1086/381156
Nelson, T., Mukai, K., Li, K.-L., et al. 2019, ApJ, 872, 86, doi: 10.3847/1538-4357/aafb6d
Ness, J. U., Osborne, J. P., Henze, M., et al. 2013, A&A, 559, A50, doi: 10.1051/0004-6361/201322415
Nguyen, T. N. T. 2018, PhD thesis, Massachusetts Institute of Technology, Cambridge, MA. http://hdl.handle.net/1721.1/119268
Nordhaus, J., & Blackman, E. G. 2006, MNRAS, 370, 2004, doi: 10.1111/j.1365-2966.2006.10625.x
Nyamai, M. M., Chomiuk, L., Ribeiro, V. A. R. M., et al. 2021, MNRAS, 501, 1394, doi: 10.1093/mnras/staa3712

Ochner, P., Moschini, F., Munari, U., & Frigo, A. 2015, MNRAS, 454, 123, doi: 10.1093/mnras/stv1867
Otero-Santos, J., Acosta-Pulido, J. A., Becerra González, J., et al. 2020, MNRAS, 492, 5524, doi: 10.1093/mnras/staa134
Owocki, S. P., & Gayley, K. G. 1997, in Astronomical Society of the Pacific Conference Series, Vol. 120, Luminous Blue Variables: Massive Stars in Transition, ed. A. Nota & H. Lamers, 121
Pablo, H., Whittaker, G. N., Popowicz, A., et al. 2016, PASP, 128, 125001, doi: 10.1088/1538-3873/128/970/125001
Page, K. L., Kuin, N. P. M., & Osborne, J. P. 2022, Universe, 8, 643, doi: 10.3390/universe8120643
Pagnotta, A., Schaefer, B. E., Clem, J. L., et al. 2015, ApJ, 811, 32, doi: 10.1088/0004-637X/811/1/32
Papadakis, I. E., & Lawrence, A. 1993, MNRAS, 261, 612, doi: 10.1093/mnras/261.3.612
Park, J., & Trippe, S. 2017, ApJ, 834, 157, doi: 10.3847/1538-4357/834/2/157
Patterson, J., Enenstein, J., de Miguel, E., et al. 2022, ApJL, 940, L56, doi: 10.3847/2041-8213/ac9ebe
Pavlenko, E. P., Mason, P. A., Sosnovskij, A. A., et al. 2018, MNRAS, 479, 341, doi: 10.1093/mnras/sty1494
Pejcha, O. 2009, ApJL, 701, L119, doi: 10.1088/0004-637X/701/2/L119
Pejcha, O., Metzger, B. D., & Tomida, K. 2016a, MNRAS, 461, 2527, doi: 10.1093/mnras/stw1481
—. 2016b, MNRAS, 455, 4351, doi: 10.1093/mnras/stv2592
Phillips, A. C., & Davis, L. E. 1995, in Astronomical Society of the Pacific Conference Series, Vol. 77, Astronomical Data Analysis Software and Systems IV, ed. R. A. Shaw, H. E. Payne, & J. J. E. Hayes, 297
Pickering, W. H. 1895, The Observatory, 18, 436
Pinheiro da Silva, L., Rolland, G., Lapeyrere, V., & Auvergne, M. 2008, MNRAS, 384, 1337, doi: 10.1111/j.1365-2966.2007.12800.x
Pininti, V. R., Bhatta, G., Paul, S., et al. 2023, MNRAS, 518, 1459, doi: 10.1093/mnras/stac3125
Poggiani, R. 2018, arXiv e-prints, arXiv:1807.07947, doi: 10.48550/arXiv.1807.07947
Pont, F., Zucker, S., & Queloz, D. 2006, MNRAS, 373, 231, doi: 10.1111/j.1365-2966.2006.11012.x
Poore, E., & Carini, M. 2023, in American Astronomical Society Meeting Abstracts, Vol. 55, American Astronomical Society Meeting Abstracts, 360.26
Popowicz, A., & Farah, A. 2020, Remote Sensing, 12, 3633, doi: 10.3390/rs12213633
Potanin, S. A., Belinski, A. A., Dodin, A. V., et al. 2020, Astronomy Letters, 46, 836, doi: 10.1134/S1063773720120038
Prialnik, D., & Livio, M. 1995, PASP, 107, 1201, doi: 10.1086/133678
Quimby, R. M., Metzger, B. D., Shen, K. J., et al. 2024, ApJ, 977, 17, doi: 10.3847/1538-4357/ad887f
Quimby, R. M., Shafter, A. W., & Corbett, H. 2021, Research Notes of the American Astronomical Society, 5, 160, doi: 10.3847/2515-5172/ac14c0
Raiteri, C. M., Villata, M., Carosati, D., et al. 2021, MNRAS, 501, 1100, doi: 10.1093/mnras/staa3561
Rani, B., Krichbaum, T. P., Lee, S. S., et al. 2017, MNRAS, 464, 418, doi: 10.1093/mnras/stw2342
Rector, T. A., Shafter, A. W., Burris, W. A., et al. 2022, ApJ, 936, 117, doi: 10.3847/1538-4357/ac87ad
Rein, H., & Liu, S. F. 2012, A&A, 537, A128, doi: 10.1051/0004-6361/201118085
Retter, A. 2002a, in American Institute of Physics Conference Series, Vol. 637, Classical Nova Explosions, ed. M. Hernanz & J. José, 279–283, doi: 10.1063/1.1518214
Retter, A. 2002b, in Astronomical Society of the Pacific Conference Series, Vol. 261, The Physics of Cataclysmic Variables and Related Objects, ed. B. T. Gänsicke, K. Beuermann, & K. Reinsch, 655, doi: 10.48550/arXiv.astro-ph/0110102
Revnivtsev, M., Churazov, E., Postnov, K., & Tsygankov, S. 2009, A&A, 507, 1211, doi: 10.1051/0004-6361/200912317
Ricker, G. R., Winn, J. N., Vanderspek, R., et al. 2015, Journal of Astronomical Telescopes, Instruments, and Systems, 1, 014003, doi: 10.1117/1.JATIS.1.1.014003
Ridden-Harper, R., Rest, A., Hounsell, R., et al. 2021, arXiv e-prints, arXiv:2111.15006, doi: 10.48550/arXiv.2111.15006
Robitaille, T., Deil, C., & Ginsburg, A. 2020, reproject: Python-based astronomical image reprojection, Astrophysics Source Code Library, record ascl:2011.023. http://ascl.net/2011.023
Rosenthal, L. J., Shen, K., Hallinan, G., et al. 2018, ApJ, 869, 7, doi: 10.3847/1538-4357/aae925
Santamaría, E., Guerrero, M. A., Toalá, J. A., Ramos-Larios, G., & Sabin, L. 2022a, MNRAS, 517, 2567, doi: 10.1093/mnras/stac2789
Santamaría, E., Guerrero, M. A., Zavala, S., et al. 2022b, MNRAS, 512, 2003, doi: 10.1093/mnras/stac563
Savitzky, A., & Golay, M. J. E. 1964, Analytical Chemistry, 36, 1627, doi: 10.1021/ac60214a047
Scargle, J. D. 1982, ApJ, 263, 835, doi: 10.1086/160554

Scaringi, S., Maccarone, T. J., Kording, E., et al. 2015, Science Advances, 1, e1500686, doi: 10.1126/sciadv.1500686
Schaefer, B. E. 2010, ApJS, 187, 275, doi: 10.1088/0067-0049/187/2/275
—. 2011, ApJ, 742, 112, doi: 10.1088/0004-637X/742/2/112
—. 2020, MNRAS, 492, 3323, doi: 10.1093/mnras/stz3325
—. 2021, Research Notes of the American Astronomical Society, 5, 150, doi: 10.3847/2515-5172/ac0d5b
—. 2022a, MNRAS, 517, 6150, doi: 10.1093/mnras/stac2900
—. 2022b, MNRAS, 517, 3640, doi: 10.1093/mnras/stac2089
—. 2023a, MNRAS, 525, 785, doi: 10.1093/mnras/stad2223
—. 2023b, MNRAS, 524, 3146, doi: 10.1093/mnras/stad735
Schaefer, B. E., Pagnotta, A., Allen, B., et al. 2010, The Astronomer's Telegram, 2452, 1
Schenker, K. 2002, in Astronomical Society of the Pacific Conference Series, Vol. 259, IAU Colloq. 185: Radial and Nonradial Pulsationsn as Probes of Stellar Physics, ed. C. Aerts, T. R. Bedding, & J. Christensen-Dalsgaard, 580, doi: 10.48550/arXiv.astro-ph/0109206
Schenker, K., & Gautschy, A. 1998, in Astronomical Society of the Pacific Conference Series, Vol. 135, A Half Century of Stellar Pulsation Interpretation, ed. P. A. Bradley & J. A. Guzik, 116
Schmidt, G. D., Liebert, J., & Stockman, H. S. 1995, ApJ, 441, 414, doi: 10.1086/175365
Schmidt, K. B., Marshall, P. J., Rix, H.-W., et al. 2010, ApJ, 714, 1194, doi: 10.1088/0004-637X/714/2/1194
Schmidt, R. E. 2021a, JAAVSO, 49, 261
—. 2021b, JAAVSO, 49, 95
—. 2021c, JAAVSO, 49, 99
—. 2022, JAAVSO, 50, 260
Schwarz, G. J., Ness, J.-U., Osborne, J. P., et al. 2011, ApJS, 197, 31, doi: 10.1088/0067-0049/197/2/31
Schwarzenberg-Czerny, A. 1996, ApJL, 460, L107, doi: 10.1086/309985
Shafter, A. W. 2017, ApJ, 834, 196, doi: 10.3847/1538-4357/834/2/196
Shafter, A. W., Clark, J. G., & Hornoch, K. 2023, Research Notes of the American Astronomical Society, 7, 191, doi: 10.3847/2515-5172/acf5e8
Shafter, A. W., Rau, A., Quimby, R. M., et al. 2009, ApJ, 690, 1148, doi: 10.1088/0004-637X/690/2/1148
Shappee, B. J., Prieto, J. L., Grupe, D., et al. 2014, ApJ, 788, 48, doi: 10.1088/0004-637X/788/1/48
Shaviv, N. J. 2001, MNRAS, 326, 126, doi: 10.1046/j.1365-8711.2001.04574.x
Shaviv, N. J. 2002a, in Astronomical Society of the Pacific Conference Series, Vol. 261, The Physics of Cataclysmic Variables and Related Objects, ed. B. T. Gänsicke, K. Beuermann, & K. Reinsch, 585
Shaviv, N. J. 2002b, in American Institute of Physics Conference Series, Vol. 637, Classical Nova Explosions, ed. M. Hernanz & J. José (AIP), 259–265, doi: 10.1063/1.1518210
Shen, K. J., & Quataert, E. 2022, ApJ, 938, 31, doi: 10.3847/1538-4357/ac9136
Shields, G. A., & Ferland, G. J. 1978, ApJ, 225, 950, doi: 10.1086/156561
Shore, S. N. 2012, Bulletin of the Astronomical Society of India, 40, 185, doi: 10.48550/arXiv.1211.3176
—. 2013, A&A, 559, L7, doi: 10.1051/0004-6361/201322470
Shugarov, S., & Afonina, M. 2021, Peremennye Zvezdy, 41, 4, doi: 10.24412/2221-0474-2021-41-14-18
Shugarov, S. Y., Goranskij, V. P., Katysheva, N. A., et al. 2005, Ap&SS, 296, 431, doi: 10.1007/s10509-005-4864-6
Sirianni, M., Mutchler, M., Gilliland, R., Biretta, J., & Lucas, R. 2007, in 2007 IEEE Radiation Effects Data Workshop, 9–15, doi: 10.1109/REDW.2007.4342533
Skowron, J., Udalski, A., Kozłowski, S., et al. 2016, AcA, 66, 1. https://arxiv.org/abs/1604.01966
Slavin, A. J., O'Brien, T. J., & Dunlop, J. S. 1995, MNRAS, 276, 353, doi: 10.1093/mnras/276.2.353
Smith, K. L., Mushotzky, R. F., Boyd, P. T., et al. 2018a, ApJ, 857, 141, doi: 10.3847/1538-4357/aab88d
Smith, K. L., Mushotzky, R. F., Boyd, P. T., & Wagoner, R. V. 2018b, ApJL, 860, L10, doi: 10.3847/2041-8213/aac88c
Sobolewska, M. A., Siemiginowska, A., Kelly, B. C., & Nalewajko, K. 2014, ApJ, 786, 143, doi: 10.1088/0004-637X/786/2/143
Sokoloski, J. L., Kenyon, S. J., Espey, B. R., et al. 2006, ApJ, 636, 1002, doi: 10.1086/498206
Sokolovsky, K. V. 2009, Peremennye Zvezdy Prilozhenie, 9, 9
Sokolovsky, K. V., & Lebedev, A. A. 2018, Astronomy and Computing, 22, 28, doi: 10.1016/j.ascom.2017.12.001
Sokolovsky, K. V., Zubareva, A. M., Kolesnikova, D. M., et al. 2019, in IAU Symposium, Vol. 339, Southern Horizons in Time-Domain Astronomy, ed. R. E. Griffin, 340–343, doi: 10.1017/S174392131800296X
Sokolovsky, K. V., Gavras, P., Karampelas, A., et al. 2017, MNRAS, 464, 274, doi: 10.1093/mnras/stw2262
Sokolovsky, K. V., Mukai, K., Chomiuk, L., et al. 2020, MNRAS, 497, 2569, doi: 10.1093/mnras/staa2104
Sokolovsky, K. V., Li, K.-L., Lopes de Oliveira, R., et al. 2022a, MNRAS, 514, 2239, doi: 10.1093/mnras/stac1440

Sokolovsky, K. V., Strader, J., Swihart, S. J., et al. 2022b, ApJ, 934, 142, doi: 10.3847/1538-4357/ac7b25

Sokolovsky, K. V., Johnson, T. J., Buson, S., et al. 2023, MNRAS, 521, 5453, doi: 10.1093/mnras/stad887

Somers, M. W., & Naylor, T. 1999, A&A, 352, 563, doi: 10.48550/arXiv.astro-ph/9910171

Sparks, W. M., & Sion, E. M. 2021, ApJ, 914, 5, doi: 10.3847/1538-4357/abf2bc

Sparks, W. M., Starrfield, S., & Truran, J. W. 1976, ApJ, 208, 819, doi: 10.1086/154668

Starrfield, S., Bose, M., Iliadis, C., et al. 2020, ApJ, 895, 70, doi: 10.3847/1538-4357/ab8d23

Starrfield, S., Iliadis, C., & Hix, W. R. 2016, PASP, 128, 051001, doi: 10.1088/1538-3873/128/963/051001

Steinberg, E., & Metzger, B. D. 2020, MNRAS, 491, 4232, doi: 10.1093/mnras/stz3300

Stetson, P. B. 1987, PASP, 99, 191, doi: 10.1086/131977

Stockman, H. S., Schmidt, G. D., & Lamb, D. Q. 1988, ApJ, 332, 282, doi: 10.1086/166652

Stone, Z., Shen, Y., Burke, C. J., et al. 2022, MNRAS, 514, 164, doi: 10.1093/mnras/stac1259

Strope, R. J., Schaefer, B. E., & Henden, A. A. 2010, AJ, 140, 34, doi: 10.1088/0004-6256/140/1/34

Suleimanov, V. F., Doroshenko, V., & Werner, K. 2019, MNRAS, 482, 3622, doi: 10.1093/mnras/sty2952

Surina, F., Hounsell, R. A., Bode, M. F., et al. 2014, AJ, 147, 107, doi: 10.1088/0004-6256/147/5/107

Takeda, L., Diaz, M., Campbell, R. D., et al. 2022, MNRAS, 511, 1591, doi: 10.1093/mnras/stac097

Tamuz, O., Mazeh, T., & Zucker, S. 2005, MNRAS, 356, 1466, doi: 10.1111/j.1365-2966.2004.08585.x

Tanaka, J., Nogami, D., Fujii, M., Ayani, K., & Kato, T. 2011a, PASJ, 63, 159, doi: 10.1093/pasj/63.1.159

Tanaka, J., Nogami, D., Fujii, M., et al. 2011b, PASJ, 63, 911, doi: 10.1093/pasj/63.4.911

Tappert, C., Schmidtobreick, L., Vogt, N., & Ederoclite, A. 2013, MNRAS, 436, 2412, doi: 10.1093/mnras/stt1747

Tarasova, T. N. 2015, Astronomy Reports, 59, 920, doi: 10.1134/S1063772915090085

Tarnopolski, M., Żywucka, N., Marchenko, V., & Pascual-Granado, J. 2020, ApJS, 250, 1, doi: 10.3847/1538-4365/aba2c7

Tempesti, P. 1975, Information Bulletin on Variable Stars, 1052, 1

Terrell, N. James, J. 1972, ApJL, 174, L35, doi: 10.1086/180944

Teyssier, F. 2019, Contributions of the Astronomical Observatory Skalnate Pleso, 49, 217

Thomas, N., Ziegler, K., & Liu, P. 2021, JAAVSO, 49, 151, doi: 10.48550/arXiv.2107.10915

Thompson, W. T. 2017, MNRAS, 470, 4061, doi: 10.1093/mnras/stx1552

Tody, D. 1986, in Society of Photo-Optical Instrumentation Engineers (SPIE) Conference Series, Vol. 627, Instrumentation in astronomy VI, ed. D. L. Crawford, 733

Tomaney, A. B., & Crotts, A. P. S. 1996, AJ, 112, 2872, doi: 10.1086/118228

Townsley, D. M., & Bildsten, L. 2005, ApJ, 628, 395, doi: 10.1086/430594

Uttley, P., McHardy, I. M., & Papadakis, I. E. 2002, MNRAS, 332, 231, doi: 10.1046/j.1365-8711.2002.05298.x

Valisa, P., Munari, U., Dallaporta, S., Maitan, A., & Vagnozzi, A. 2023, arXiv e-prints, arXiv:2302.04656, doi: 10.48550/arXiv.2302.04656

Vallely, P. J., Kochanek, C. S., Stanek, K. Z., Fausnaugh, M., & Shappee, B. J. 2021, MNRAS, 500, 5639, doi: 10.1093/mnras/staa3675

van den Bergh, S., & Younger, P. F. 1987, A&AS, 70, 125

VanderPlas, J. T. 2018, ApJS, 236, 16, doi: 10.3847/1538-4365/aab766

Vanderspek, R., Doty, J. P., Fausnaugh, M., et al. 2018, TESS Instrument Handbook (TESS Science Office). https://archive.stsci.edu/files/live/sites/mast/files/home/missions-and

Vanlandingham, K. M., Starrfield, S., Wagner, R. M., Shore, S. N., & Sonneborn, G. 1996, MNRAS, 282, 563, doi: 10.1093/mnras/282.2.563

Vaughan, S. 2010, MNRAS, 402, 307, doi: 10.1111/j.1365-2966.2009.15868.x

Vaughan, S., Edelson, R., Warwick, R. S., & Uttley, P. 2003, MNRAS, 345, 1271, doi: 10.1046/j.1365-2966.2003.07042.x

Vaughan, S., Uttley, P., Markowitz, A. G., et al. 2016, MNRAS, 461, 3145, doi: 10.1093/mnras/stw1412

Vogt, N. 1990, ApJ, 356, 609, doi: 10.1086/168866

von Essen, C., Lund, M. N., Handberg, R., et al. 2020, AJ, 160, 34, doi: 10.3847/1538-3881/ab93dd

von Neumann, J. 1941, Ann. Math. Statist., 12, 367, doi: 10.1214/aoms/1177731677

—. 1942, Ann. Math. Statist., 13, 86, doi: 10.1214/aoms/1177731645

Wehrle, A. E., Wiita, P. J., Unwin, S. C., et al. 2013, ApJ, 773, 89, doi: 10.1088/0004-637X/773/2/89

Weiss, W. W., Zwintz, K., Kuschnig, R., et al. 2021, Universe, 7, 199, doi: 10.3390/universe7060199

Wolf, W. M., Townsend, R. H. D., & Bildsten, L. 2018, ApJ, 855, 127, doi: 10.3847/1538-4357/aaad05

Woudt, P. A., Steeghs, D., Karovska, M., et al. 2009, ApJ, 706, 738, doi: 10.1088/0004-637X/706/1/738

Yuan, F., & Akerlof, C. W. 2008, ApJ, 677, 808, doi: 10.1086/529040

Zackay, B., Ofek, E. O., & Gal-Yam, A. 2016, ApJ, 830, 27, doi: 10.3847/0004-637X/830/1/27

Zhang, E., Robinson, E. L., Stiening, R. F., & Horne, K. 1995, ApJ, 454, 447, doi: 10.1086/176496

Zuckerman, L., De, K., Eilers, A.-C., Meisner, A. M., & Panagiotou, C. 2023, MNRAS, 523, 3555, doi: 10.1093/mnras/stad1625

Zwitter, T., & Munari, U. 2000, An introduction to analysis of single dispersion spectra with IRAF